



JGR Planets

RESEARCH ARTICLE

10.1029/2021JE007169

Key Points:

- Pioneer-Voyager-Galileo occultations reveal a complex ionosphere, with peak densities inconsistent with photo-chemical-equilibrium theory
- Total electron content values correlate with solar flux changes over solar cycle time frames
- Average electron density patterns reveal a three-layer profile, with occasional low-altitude highly structured densities

Supporting Information:

Supporting Information may be found in the online version of this article.

Correspondence to:

C. Narvaez, cnarvaez@bu.edu

Citation:

Mendillo, M., Narvaez, C., Moore, L., & Withers, P. (2022). Jupiter's enigmatic ionosphere: Electron density profiles from the Pioneer, Voyager, and Galileo radio occultation experiments. *Journal of Geophysical Research: Planets*, 127, e2021JE007169. https://doi.org/10.1029/2021JE007169

Received 20 DEC 2021 Accepted 8 MAR 2022

© 2022. American Geophysical Union. All Rights Reserved.

Jupiter's Enigmatic Ionosphere: Electron Density Profiles From the Pioneer, Voyager, and Galileo Radio Occultation Experiments

Michael Mendillo¹, Clara Narvaez¹, Luke Moore¹, and Paul Withers¹

¹Center for Space Physics, Boston University, Boston, MA, USA

Abstract Radio occultation experiments on the Pioneer and Voyager missions obtained the first seven electron density profiles $N_a(h)$ of Jupiter's ionosphere. We use the five complete $N_a(h)$ observations to assess patterns and processes linked to photo-chemical-equilibrium (PCE) theory, modeled previously to be the domain below $\sim 1,000$ km. We find that the $N_{\rm s}(h)$ profiles are highly structured and identification of the maximum electron density and its height do not follow PCE expectations for layers produced by the Sun's soft X-rays and extreme ultraviolet. Pre-dawn profiles often show larger electron densities than dusk-side profiles, inconsistent with simple chemical decay throughout nighttime. We examined total electron content (TEC) values, defined as $N_s(h)$ integrated up to a 3,500 km height, and found statistically significant TEC correlations (correlation coefficient ~ 0.85) with solar fluxes over solar cycle time scales. The subsequent set of 25 $N_s(h)$ profiles obtained during the Galileo mission confirmed all of the variability patterns found by Pioneer and Voyager. Most notable was a weaker solar cycle pattern for TEC. Yet, different solar cycle characteristics during the three missions cannot explain their different values for TEC. Average $N_{c}(h)$ profiles from the early missions (P10-11; V1-2) revealed a three-layer system that was confirmed by average Galileo results. Models using faster electron-ion recombination caused by vibrationally excited H₂ converting atomic ions to molecular ions could lead to enhanced removal of plasma near $\sim 1,000$ km, and thus the topside layer formation that often appears at ~1,500 km, while XUV radiation likely produces the two lower layers in the PCE domain.

Plain Language Summary Satellites sent to Jupiter use radio signals to transfer information back to Earth. If these radio signals are sent when the satellite starts to pass behind Jupiter, and then emerges from behind it, distortions of the radio waves can be used as a diagnostic tool for studying the planet's ionosphere (the electrons and ions within its upper atmosphere). This paper offers new analyses and interpretation of the first seven "radio occultation experiments" conducted by the Pioneer and Voyager satellites in 1973-4 and 1979. We find that the electron density distribution with height is so variable that no consistent pattern emerges for the planet's maximum electron density and its height of occurrence. However, when we examined the sum all of the electron densities up to 3,500 km, the total electron content, we found it to show strong control by the Sun's photon flux during years of low and high solar activity. Decades later, when the Galileo mission conducted similar experiments (1995–2001), the variabilities of peak densities and the overall ionosphere were similar, but with reduced magnitudes. Modeling studies are needed to understand how solar photons and energetic particles impinging upon the upper atmosphere can explain the complex ionospheric system at Jupiter.

1. Introduction—Context of Comparative Ionospheres

1.1. Overview

The first measurement of another planet's ionosphere occurred using Mariner IV's radio occultation experiment (ROX) at Mars in 1965 (Kliore et al., 1965). Mariner V then conducted the next planetary ROX at Venus (Kliore et al., 1967)—thus completing the first opportunities to conduct comparative ionosphere research for the inner solar system. The application of the radio occultation method to the outer planets first occurred with the Pioneer-10 fly by of Jupiter in December 1973 (Fjeldbo et al., 1975). Subsequent ionospheric observations at Jupiter were conducted during the Pioneer-11, Voyager-1, and -2 flybys, and decades later by ROX studies using the orbiting Galileo spacecraft. This paper deals with a new look at the totality of ROX electron density profiles, $N_e(h)$, at Jupiter.

MENDILLO ET AL. 1 of 25



1.2. Background

The vertical structure of Jupiter's ionosphere is not currently understood. Using the terrestrial planets for context, the overall shape of a vertical profile of electron density contains a small number of distinctive layers, and the densities, altitudes, and widths of such layers can be interpreted to shed light on ion production rates, ion-electron loss mechanisms, plasma composition, and neutral atmospheric structure (Bauer & Lammer, 2004; Rishbeth & Garriott, 1969; Schunk & Nagy, 2009; Witasse et al., 2008). Yet the vertical structure of Jupiter's ionosphere is remarkably variable across observations. As stated by Yelle and Miller (2004): "The characteristics of the electron density profiles do not correlate with any obvious geophysical parameters."

Reviews of Jupiter's ionosphere have concluded that the published electron density profiles "seem to fall in two general classes. In one, the peak electron density is located at an altitude around 2,000 km, and in the other the electron density peak is near 1,000 km" (Nagy & Cravens, 2002). The first class is more common than the second class. Yelle and Miller (2004) agreed with a division into two classes, but favored characteristic peak altitudes of "1,500–2,000" km and "below 1,000 km." Yet it is not clear why these two classes of profiles exist. As Nagy and Cravens (2002) ruefully noted: "The different peaks may be the result of a combination of different major ionizing sources (extreme ultraviolet, EUV) versus soft X-ray versus particle impact and/or different ion chemistries."

The primary aim of this article is to examine the layered structure of Jupiter's ionosphere in order to assess whether the layer properties follow the trends expected for photochemical equilibrium conditions. We contrast these findings with the integral of the electron density profile (called total electron content, TEC) to see if total plasma populations offer more consistent patterns than found with individual layers.

In Section 2, we present a brief overview of the photo-chemical processes that lead to an ionospheric profile having specific layers. Section 3 deals with the initial seven ionospheric profiles and their layers at Jupiter obtained during the Pioneer (1973-74) and Voyager (1979) missions. Using the solar radio flux at 10.7 cm (F10.7) observed at Earth to characterize solar activity, the Pioneers were at solar minimum [<F10.7 > $_{1 \text{ AU}} \sim$ 77] and Voyagers at solar maximum [<F10.7 > $_{1 \text{ AU}} \sim$ 170]. The morphology patterns they exhibit thus provide information on solar cycle effects. In Section 4 we present the larger set of radio occultation profiles (25) from the Galileo mission that also spans solar min/max conditions (1995–2001). Section 5 characterizes the combined set of thirty-two Pioneer-Voyager-Galileo $N_e(h)$ profiles. In Section 6 we offer analyses to see if their maximum electron densities and total electron contents conform to expectation from photo-chemical-equilibrium (PCE) processes. Our summary appears in Section 7, with questions to address in future studies appearing in Section 8.

2. Review of Photo-Chemical-Equilibrium Characteristics in an Ionosphere

2.1. Approaches to Semi-Empirical Modeling

Basic models of planetary ionospheres address the vertical structure of electron density that results from solar photons ionizing a small fraction of the neutral gases in a planet's upper atmosphere. Such processes were first investigated at Earth (Chapman, 1931a, 1931b). As shown in subsequent textbooks (e.g., Bauer & Lammer, 2004; Rishbeth & Garriott, 1969; Schunk & Nagy, 2009), the solar irradiance (photon flux vs. wavelength) of relevance consists of EUV and soft X-rays (collectively called XUV). The ionization produced by XUV photons occurs at different heights, with soft X-rays responsible for a low altitude peak (E-layer at Earth, V1 and M1 layers at Venus and Mars, respectively). The EUV layer appears above, designated F1 at Earth and V2 and M2 at Venus and Mars. The EUV produced layers generally have higher electron densities than the X-ray produced layers. The plasma produced is then subject to a continuity equation linking production (*P*), chemical loss (*L*) and changes in plasma density due to motion (*M*):

$$\frac{dN_e}{dt} = \text{Production}(P) - \text{Loss}(L) + \text{Motion}(M) \tag{1}$$

For times when $N_{\rm e}$ changes slowly, and changes due to dynamics are minimal (e.g., at mid-day), the first and fourth terms in Equation 1 are small and thus $P \sim L$, a condition called PCE. Perhaps surprisingly, when more rapid changes in $N_{\rm e}$ occur (e.g., after sunrise and pre-sunset), the time constants for photo-ionization and chemical loss can still be smaller than for dynamics and the P = L condition continues to hold. This PCE dominance occurs when the photons responsible for ionization encounter a neutral atmosphere so dense that the processes of

MENDILLO ET AL. 2 of 25



ionization, ion-neutral chemistry, and electron-ion recombination occur "in place"—that is, at rates much faster than dynamical processes. Under such conditions, production is proportional to the overhead solar flux (F_{sun}), with spatial/temporal variations characterized by the solar zenith angle (SZA), and thus $P \sim F_{sun} \times \cos(SZA)$. Loss occurs at the ion-electron recombination rate (α), $L \sim \alpha N_e^2$. Equating P and L results in

$$N_{\rm e}^2 \sim F_{\rm sun} \times \cos({\rm SZA})$$
 (2)

This relationship is expected to hold at all heights where the photo-chemical formalism is dominant. The observed height (h_{max}) of maximum electron density (N_{max}) may be in the PCE domain or above it.

When observations are tested using the parameterization in Equation 2, a high correlation coefficient (CC > 0.90) occurs at Earth, Mars, and Venus (Mendillo et al., 2016, 2020).

For Saturn, the situation is very different. At best, the application of Equation 2 yields a $CC \sim 0.50$ (Mendillo et al., 2018). The reason for "poorly behaved" layers at Saturn is that the PCE conditions are affected by non-local processes, in particular, large influxes of water and other external contaminants that modify atmospheric chemistry (Moore et al., 2018). Thus, if Saturn did not have icy rings or the moon Enceladus as sources of infalling material, the expectation could be another planetary example of two dominant PCE-controlled ionospheric layers.

Our approach to semi-empirical modeling of Jupiter's ionosphere adopts the same protocols we used for Venus, Mars, and Saturn. The goal is to specify values of the maximum electron density $(N_{\rm max})$ and total electron content (TEC = $\int N_e(h) \, dh$) as a function of coupled solar flux and SZA for daytime conditions (SZA <90°), as embodied in Equation 2. For PCE controlled ionospheric layers, TEC is proportional to $N_{\rm max} \times H$ (neutral scale height), as described in Wright (1960), and thus the expectation is that TEC will follow the same functional relationship shown in Equation 2. This approach would start to break down, of course, if there are layers with both PCE and dynamics. Finally, given that Jupiter's orbit is elliptical (eccentricity = 0.048), we will apply Equation 2 to conditions at the planet's mean distance from the Sun ($d = 5.20 \, {\rm AU}$). For solar flux, Equation 2 handles conditions away from the sub-solar point via the cos (SZA) term. For orbital distance corrections, $F_{\rm sun}$ varies as $1/d^2$, and thus $N_e \sim 1/d$.

All other processes and parameters involved in PCE conditions that contribute to variability of $N_{\rm max}$ and TEC are considered to be secondary. These include changes in the composition of the neutral atmosphere, uncertainties about ionization cross sections, secondary ionization rates, and chemical reaction rates—plus all forms of dynamics (neutral and plasma). The fact that success can be achieved for Venus and Mars using this remarkably simple approach is testimony of how dominant PCE conditions can be in a plasma composed of molecular ions and electrons in a very dense neutral atmosphere. Yet, giant planet ionospheres have abundant atomic ions (H⁺) as well as molecular ions (H₂⁺ and H₃⁺), and thus the PCE approach for Jupiter will face increased restraints. Given that the terrestrial ionosphere also has atomic ions within its dominant region (F2-layer), the Earth-Jupiter analogy is a particularly interesting case of comparative ionospheres.

2.2. Specific Methodology

With observations of solar irradiance not available at Jupiter, the long-standing practice is to characterize solar output by the Sun's radio flux at 10.7 cm (F10.7) observed on a daily basis at Earth. To relate these proxy solar fluxes measured at Earth to ionospheric observations made at Jupiter, the positions of both planets in their elliptical orbits must be taken into account. The protocol adopted is to transform all observations (using flux $\sim 1/d^2$ and $N_e \sim 1/d$) to an equivalent circular orbit for Jupiter (5.2 AU), determine the "rotated-Sun" date (when the side of the Sun facing Jupiter was observed at Earth), and form the effective solar flux ($F_{\rm eff}$, see Schunk & Nagy, 2009) using

$$F_{\text{eff}} = \frac{F10.7_{\text{(day)}} + \langle F10.7 \rangle_{(81-\text{day})}}{2} \quad \text{[all at d = 5.2 AU]}$$

The PCE equations at that fixed distance from the Sun are then used to formulate the PCE model. This protocol is fully described in our study of Venus' ionosphere (Mendillo et al., 2020). The end result for maximum electron density (N_{max}), that also holds for TEC, is

$$N_{\rm max}$$
 and TEC $\sim \sqrt{F_{\rm eff} \times \cos({\rm SZA})}$ (4)

MENDILLO ET AL. 3 of 25



Table 1List of Pioneer and Voyager Occultations and Their Properties as Measured at Jupiter

								Electron density 10 ¹⁰ (e ⁻ /m ³)			TTP Co
Occulta-tion	Date	Rotated-Sun date	Lat (°)a	Lon (°)ª	SZA (°)	Jupiter-Sun distance (AU)	Rotated flux effective (1AU)	$N_{\rm max}$	$\overline{[N_e]}$ <1,000 km	Height $(km)^b$ of N_{max}	TEC ^c 10 ¹⁶ (e ⁻ /m ²)
P10N, Duske	4 December 1973	13 December 1973	28	315	81.5	5.1	77.2	26.0	2.7	654	7.0
P10X, Dawne	4 December 1973	13 December 1973	58	100	94.4	5.1	77.2	34.8	3.2	1,199	8.6
P11N, Duskf	3 December 1974	9 December 1974	-79	97	92.5	5.0	75.8	16.8	5.0	1,162	8.6
V1N, Duskg	5 March 1979	8 March 1979	-12	297	82.0	5.3	183.9	2.1 ^h		2,130	2.8
V1X, Dawn ^g	5 March 1979	8 March 1979	1	46	98.0	5.3	183.9	24.3 ^h		1,898	16.9
V2N, Duski	9 July 1979	20 July 1979	-67	105	88.1	5.3	159.6	34.4	10.7	796	15.3
V2X, Dawni	9 July 1979	20 July 1979	-50	212	94.4	5.3	159.6	23.3	0.7	2,077	29.5

^aLatitudes and longitudes are in System III, 1965.0. ^bAll heights are referenced to the 1 bar level. ^cTEC was integrated from the bottom of the profile up to 3,500 km and thus with different column extents. For altitudes with data gaps, where retrieval yields negative electron density values, TEC is calculated by interpolating the positive values above and below. Alternatively, zero values for electron could have been assumed, the resulting TEC would differ by a very small amount, an average of 0.03 TEC units. ^dAverage electron density below 1,000 km, calculated whenever the profile extends down to at least 850 km and five or more values are available for averaging. ^eFjeldbo et al. (1975). ^fWoo and Yang (1978). ^gEshleman et al. (1979). ^hM_{max} values shown are only for information purposes---not included in analyses due to lack of data at low heights. ⁱHinson et al. (1998).

We do not use the grazing incidence formula in place of $\cos(SZA)$ because it requires prior knowledge of the scale height of the neutral atmosphere for each profile (Rishbeth & Garriott, 1969). Fitting Equation 4 to observational data sets (N_{max} , TEC, F_{eff} , and SZA) yields the best-fit linear correlations,

$$N_{\text{max}}$$
 and TEC = $C_1 \sqrt{F_{\text{eff}} \times \cos(\text{SZA})} + C_2$ (5)

This equation is suitable for all daytime conditions given by SZA = 0° to 90° . Moreover, it provides "default" values of N_{max} and TEC beyond the solar terminators (sunset and dawn). That is, N_{max} or TEC = C_2 , when the cosine parameter (with SZA = 90°) eliminates the first term in the equation.

The success of Equation 5 for semi-empirical modeling of the PCE ionospheric patterns found at Mars and Venus—with partial success at Saturn—has been achieved using $N_e(h)$ ROX data sets numbering in the thousands for Mars, hundreds for Venus and 64 at Saturn. In this study, we investigate the next largest $N_e(h)$ data set for a planet (Jupiter). We begin with the seven "discovery-mode" $N_e(h)$ profiles obtained from the Pioneer and Voyager missions between 1973 and 1979, and then treat the 25 $N_e(h)$ profiles obtained during the Galileo mission (1995–2001).

3. Pioneer and Voyager Era Observations

3.1. Overview

Table 1 summarizes the geometrical and plasma properties of the radio occultation profiles obtained during the Pioneer and Voyager fly-by observations. As occurs for ROX profiles of outer planets, all of the SZAs are close to 90°—perhaps the most difficult local times for modeling ionospheres. Note that the profiles labeled "Dawn" all have solar zenith angles greater than 90°, that is, the ionosphere was observed prior to local "surface" sunrise. Yet, given the large vertical extent of the Jovian ionosphere (heights to 3,500 km), solar photons can obviously impinge upon the upper atmosphere even when SZAs are above 90° at the surface. Note that the four profiles labeled "Dusk" have SZA values both above and below 90°.

To compare $N_e(h)$ patterns from different missions requires that the same height system be used. Radio occultations from Pioneer produced electron density profiles with zero altitude at the level where the lower neutral atmosphere has a refractivity of 10 (Fjeldbo et al., 1975), which corresponds to 1-mbar (Eshleman et al., 1979). The altitudes for Voyager electron density profiles were also quoted to be above the 1-mbar level (McConnell et al., 1982). However, in a departure from previous ROX results, Hinson et al. (1997) quoted heights above the

MENDILLO ET AL. 4 of 25



1- bar level for Galileo's $N_e(h)$ profiles. In order to have a uniform and consistent reference height, that is, 1-bar level, Pioneer and Voyager heights for electron density profiles have been adjusted by adding 160 km—the height interval between 1-mbar and 1-bar (Lindal et al., 1981).

The first major review of the Pioneer/Voyager epoch-making profiles appeared in McConnell et al. (1982). Their data analysis was extensive and their modeling comprehensive—addressing dusk-versus-dawn diurnal patterns as well as low-versus-high solar flux conditions. An important aspect of their model was that it included two key reactions that occur in giant planet ionospheres that transform the major ions produced (H^+ , H_2^+) into ions with faster recombination rates: H^+ to H_2^+ and H_2^+ to H_3^+ :

$$H^+ + H_2(\nu \ge 4) \to H_2^+ + H$$
 (6)

$$H_2^+ + H_2 \to H_3^+ + H$$
 (7)

There are interesting ramifications for Equation 6 due to the requirement that molecular H_2 must be in the \geq 4th vibrational state for the reaction to proceed. If the energetics within the Jovian ionosphere do not allow Equation (6) to dominate, and given that the atomic ion recombination rate with electrons ($H^+ + e^- = H$) is slow, long-lived atomic hydrogen ions remain, and especially so at high altitudes where H_2 decreases more rapidly that H. Moreover, with Jupiter's rotation rate of \sim 10 hr, nighttime decay lasts for only five hours. Thus, a post-sunset atomic ion ionosphere would persist in much the same way that O^+ ions do in the terrestrial F2-layer. Finally, the McConnell et al. (1982) simulations pointed out that solar production maximizes below 1,000 km, and we use that altitude to define the top of the PCE domain. The higher altitude layers found at Jupiter must involve a combination of photo-chemical and dynamical processes, as occurs with the F2-layer at Earth.

During the same period as the McConnell et al. (1982) study, Strobel and Atreya (1983) offered a second comprehensive summary of approaches to modeling the Jovian ionosphere. Strobel and Atreya concluded that "Comparison of Pioneer and Voyager electron concentration profiles suggests that Jupiter's ionosphere is at least as complex and variable as the Earth's ionosphere. Of potential importance but still poorly understood is the multi-layered structure of Jupiter's ionosphere."

Subsequent modeling studies were conducted by many groups (e.g., Cravens, 1987; Maurellis & Cravens, 2001; Waite et al., 1997) that achieved broad success for specific profiles. Yet, with many free parameters to adjust, and large uncertainties about the neutral atmosphere to be ionized, constraints on model-data comparisons were not strong. A good example of exploring how dynamical processes (diffusion and/or neutral winds) compete with PCE processes (including Equation 6) appears in Majeed et al. (1999). The most recent review of Jupiter's ionosphere was made by Yelle and Miller (2004). It is their conclusion—"As was first noted by McConnell et al. (1982), the characteristics of the electron density profiles do not correlate with any obvious geophysical parameters"—that motivates a new approach. Our goal is to go beyond the elusive aspect of understanding the observed maximum electron density patterns found by Pioneer and Voyager in favor of height-integrated TEC patterns. Given the small number of published profiles per mission, we will discuss them individually and by category (e.g., solar max vs. solar min)—with a new emphasis on height-integrated results. This will set the context for the 25 ROX profiles obtained during the Galileo mission (1995–2001) that will be discussed in the following section.

3.2. Initial Observations of Jupiter's Ionosphere by Pioneer-10 and -11 Fly-bys

The first pair of Jovian electron density profiles was observed on 4 December 1973 using radio occultation techniques during the Pioneer 10 fly-by (Fjeldbo et al., 1975). Figures 1a and 1b show these milestone data sets. Observations during the immersion phase (color-coded red) occurred in late afternoon ("dusk" in Table 1), with emersion data (color-coded blue) taken prior to surface sunrise ("dawn" in Table 1). The $N_e(h)$ profiles revealed a surprisingly complex plasma system composed of many ionospheric layers. In retrospect, and as discussed later, the phrase "profiles highly structured in height" or "profiles with multiple local maxima" would have been preferable given that the concept of an "ionospheric layer" historically referred to a *consistent* altitude pattern of ions and electrons produced by photo-chemical and dynamical processes.

Standard approaches to processing radio occultation data involve a baseline correction that depends upon the behavior of observed quantities at altitudes above the top of the ionosphere (see recent review of ROX methods

MENDILLO ET AL. 5 of 25

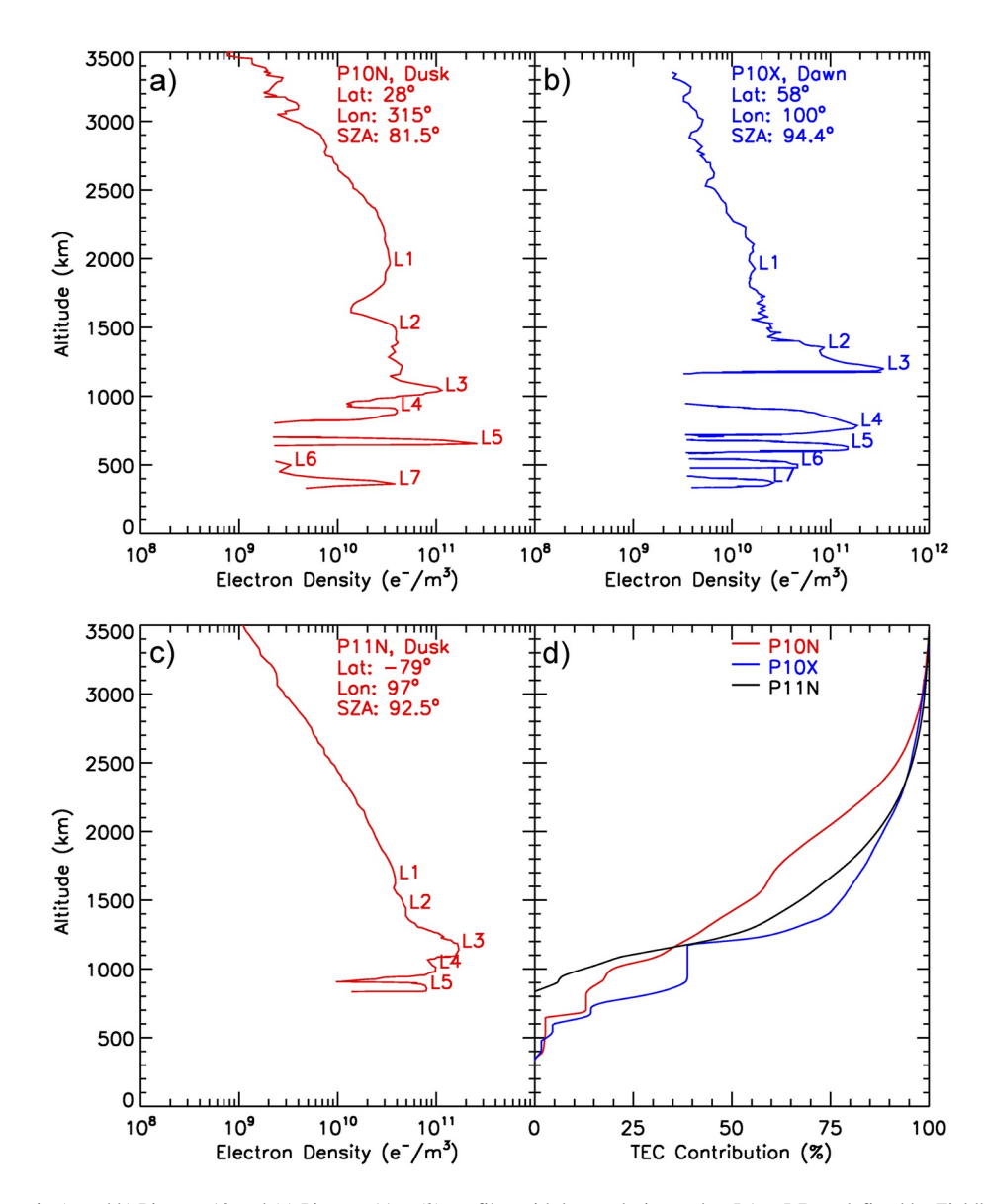


Figure 1. (a and b) Pioneer-10 and (c) Pioneer-11 $N_e(h)$ profiles with layers designated as L1 to L7, as defined by Fjeldbo et al. (1975) and Woo and Yang (1978). Longitudes are given in Table 1. For altitudes with data gaps, where occultation retrieval yields negative electron density values, total electron content (TEC) values shown in Table 1 are calculated by interpolating between the positive values above and below, for example, as shown between L4 and L3 for P10X. Using zero values within data gaps has a minimal effect since the interpolated values are a few orders of magnitude lower than the positive values shown. Panel (d) gives the TEC "contribution profiles" (percent of TEC) with height up to the top altitude portrayed.

and references in Withers et al. [2020]). Fjeldbo et al. (1975) noted challenges in the implementation of this baseline correction for the Pioneer-10 ingress profile and reported two different versions of the derived electron density profile (their Figures 2 and 5). Here we adopted the profile from their Figure 5 that reaches $\sim 10^9 \text{ e}^-/\text{m}^3$ between 3,000 and 4,000 km, versus their Figure 2 profile that has N_e values higher than $\sim 10^9 \text{ e}^-/\text{m}^3$ beyond $\sim 4,000 \text{ km}$.

Fjeldbo et al. (1975) also considered other aspects of radio propagation that affect such measurements—the most serious problems being due to multi-path propagation and radio amplitude and phase scintillation produced by small-scale irregularities within the ionosphere of the planet with the harshest radiation environment. The immediate implication is that the processes of photo-ionization and chemical recombination may not be the only (or even the dominant) processes needed for scientific interpretation. Among non-PCE sources considered

MENDILLO ET AL. 6 of 25



are ionizations by energetic particle precipitation (e.g., Cravens, 1987; Waite et al., 1983). At Earth, this not a planet-wide process, but one confined to "auroral zone" latitudes generally above ~65° magnetic (Schunk & Nagy, 2009). At Mars, energetic particle sources can lead to structured, non-solar produced plasma primarily near crustal magnetic field locations. At Venus, with no global magnetic field, non-solar photon sources are essentially irrelevant to observed ionospheric patterns for "daytime" conditions characterized by SZA <90°.

In addition to precipitation effects, other sources of structured plasma patterns are signatures arising from plasma instabilities (Kelley, 1989; Matcheva et al., 2001), atmospheric gravity waves, hydrocarbon layers, and metallic ion layers. Successful modeling studies were conducted by Matcheva et al. (2001), and later by Majeed et al. (2004). Such features in the lower ionosphere add considerable uncertainty to the identification of specific layers related to XUV-driven PCE processes occurring at the same altitudes. Of particular concern is the specification of the maximum electron density for a given profile—should it be above the height of structuring, or should $N_{\rm max}$ for a narrow low-altitude layer still serve as the quantitative definition of peak electron density?

At Earth, occasional enhancements of the E-layer occur between ~ 90 and 120 km that are unrelated to the photo-ionization of ambient neutrals. They are called Sporadic-E events or Es-layers (Schunk & Nagy, 2009). It is not unusual for Es peak densities to exceed the highest electron density in the F2-layer (called blanketing Es conditions). Because they are not the result of PCE processes, they are not considered to be the true $N_{\rm max}$ of an electron density profile, but rather an anomalous profile feature at low altitudes. Such Es-layers are narrow in altitude (typically 0.5–2.0 km) and they occur at all latitudes. They can arise from multiple sources: metallic ions and electrons produced from meteor ablation, and/or from wind shears, tides and gravity wave distortions of ambient plasma. Their severe spatial gradients can result in plasma irregularities that cause significant effects upon radio propagation. At Jupiter, the low-altitude layering is of particular concern because it occurs in the very region of maximum photo-ionization (not the case for Es at Earth). Jupiter thus presents a major challenge to the identification of $N_{\rm max}$ within a truly complex system.

3.3. Specific Characteristics of Jupiter's Electron Density Profiles

As shown in Figure 1, Fjeldbo et al. (1975) offered labels to identify the multiple layers found—seven in total—for both immersion and emersion. The layer designations shown in Figures 1a and 1b pertain to observations that occurred \sim 60 min apart on opposite sides of the planet (see Table 1 in Woo and Yang [1978]). The ability to identify these seven specific layer peak densities and altitudes in two widely separated locations added confidence to the notion of spatial stability of such a highly structured ionosphere. The subsequent Pioneer-11 profile (Figure 1c) conformed to this pattern—adding further credibility to the temporal consistency of a Jovian ionosphere being a plasma system of five-to-seven-layers. Yet, it is worth noting that no model studies were conducted that produce a $N_c(h)$ profile at Jupiter with five to seven layers.

There are obvious difficulties in attempts to define consistent peak layer height ranges and densities in Figure 1: N_{max} and h_{max} are at L5 at dusk for Pioneer-10, at L3 for Pioneer-10 (dawn), and at L3 (dusk) again for Pioneer-11. This variability led us to explore alternate approaches from using N_{max} as the single parameter most useful for representing a profile at Jupiter. Specifically, we will introduce the use of the TEC calculated for each $N_e(h)$ profile. Having TEC as the single quantitative value to characterize each profile offers a different approach to understanding the overall Jovian ionospheric system.

There is a considerable history of studying TEC at Earth and a few other planets in the solar system. At Earth, observations of TEC obtained by radio science experiments using the constellation of Global Positioning System satellites are the dominating ionospheric diagnostic in use today (Materassi et al., 2019). With over 6,000 stations distributed globally, and each site observing 4–6 satellites at any time, TEC values are available every minute to form global maps of TEC. For planetary ionospheres, the first use of TEC data occurred with studies at Mars. Radio occultation profiles obtained by the Mars Global Surveyor satellite (Hinson et al., 1999) were integrated to form TEC values for analyses (Mendillo et al., 2004). The Mars Express mission used an orbiting radar (Gurnett et al., 2005; Picardi et al., 2005; Safaeinili et al., 2003, 2007) to produce TEC data sets that enabled fundamental ionospheric science at Mars (Cartacci et al., 2013; Mendillo et al., 2013). The radar on the Mars Reconnaissance Orbiter also provided global information about TEC at Mars (Campbell & Watters, 2016; Mendillo et al., 2017).

MENDILLO ET AL. 7 of 25



TEC has also been studied at Saturn (Mendillo et al., 2018) and Venus (Mendillo et al., 2020) using height-integrated ROX profiles.

To form TEC values at Jupiter, the limits of integration (h_{low} , h_{high}) have to be the same so that comparisons are not influenced by different vertical overage. Figure 1 illustrates the problem in that the profile from Pioneer 11, shown in panel (c), does not have full bottom-side coverage. To address this issue, we show in panel (d) the TEC contribution functions, that is, the build-up with altitude of the integration. Note that the lowest heights having considerable structure contribute only a small portion of the TEC. The $\sim 50\%$ contribution heights are slightly above 1,000 km and thus the PCE domain contributes at least half of a TEC value—thus offering an expectation that TEC will follow PCE trends. Table 1 shows the TEC values formed from the three profiles in Figure 1.

The Pioneer-10 $N_e(h)$ profiles have the following characteristics worthy of comment and discussion (with electron densities in units of 10^{10} e⁻/m³ and TEC units of 10^{16} e⁻/m², called TECU):

- 1. The $h_{\rm max}$ value at dawn (L3 at 1,199 km) is higher than at dusk (L5 at 654 km), consistent with enhanced decay of the bottom-side ionosphere during the nighttime hours.
- 2. The N_{max} value at dawn (34.8 units) is greater than the value at dusk (26.0 units), inconsistent with nighttime decay yielding the lowest electron densities prior to local sunrise.
- 3. The TEC value at dawn (8.6 TECU) is also greater than the value at dusk (7.0 TECU), inconsistent with the anticipated diurnal pattern from basic PCE.

Thus, while different latitudes were sampled, the second and third characteristics are the ones of concern for Pioneer-10.

While the Pioneer-11 ROX was conducted a year later (3 December 1974) using both emersion (dusk) and immersion (dawn) opportunities, the only published profile from Pioneer-11 is for the dusk sector (Woo & Yang, 1978). It occurred at high latitude (79°S) and is Figure 1c. This dusk-side profile appeared to have five of the seven layers as identified by Chen (1981). The height of maximum electron density (1,162 km) is twice the value for the dusk profile from Pioneer-10 (654 km); the $N_{\rm max}$ value (16.8 units) is less than the Pioneer-10 dusk value of 26 units—perhaps consistent with solar input differences at a high latitude (79°S) versus a middle latitude (28°N) location.

For TEC, the dusk-only value of 8.6 TEC units from Pioneer-11 is in basic agreement with expectations from Pioneer-10. As shown in Table 1, solar flux values during the Pioneer fly-bys were typical of a deep solar minimum period, and thus the $N_e(h)$ profiles obtained can be taken as representative of baseline PCE conditions for Jupiter's ionosphere (but with significant inconsistencies noted).

3.4. Voyager-1 and -2 Observations of the Jovian Ionosphere

The Voyager-1 and -2 fly-bys occurred 5 years after those of Pioneer-10/11, and thus offered ionospheric patterns under strong solar maximum conditions. The Voyager-1 encounter occurred on 5 March 1979 with its dusk and dawn observations at low latitudes $(-12^{\circ}, 1^{\circ})$. The two $N_e(h)$ profiles obtained suffered from incomplete coverage in altitude—with data obtained only for heights above 1,500 km. These profiles are shown in Figure 2a. The apparent peak electron densities occurred at 2,130 km and 1,898 km, respectively, for dusk and dawn—but the lack of observations below 1,500 km prevents a rigorous evaluation of these profiles for reliable values of N_{max} or TEC. What can be said is that the N_{max} values reveal a dawn value that is a factor of 10 larger than the dusk value. These are not conditions consistent with electron densities controlled by PCE processes. While modeling attempts were explored (e.g., Atreya et al., 1979), the conclusion must be that the Voyager-1 ROX partial profiles present considerable challenges for understanding ionospheric physics at Jupiter.

The Voyager-2 mission's encounter with Jupiter occurred 4 months later on 9 July 1979, with results obtained at upper mid-latitudes in the southern hemisphere (67°S, 50°S). The $N_e(h)$ profiles obtained are shown in Figures 2b and 2c. Perhaps the first item to note is that the multi-layer designations introduced for the Pioneer-10 and -11 results (Figure 1) were never used again. The dusk profile (red) is somewhat similar in appearance to the observation at dusk made by Pioneer-11. There is a clear h_{max} at 796 km with a high N_{max} value (34.4 × 10¹⁰ e⁻/m³). At greater heights, a local N_e maxima occurs at ~1,200 km, but there are no additional layers between 500 and 2,000 km. For the dawn profile, most striking is that the $N_e(h)$ pattern below 1,500 km is highly structured.

MENDILLO ET AL. 8 of 25

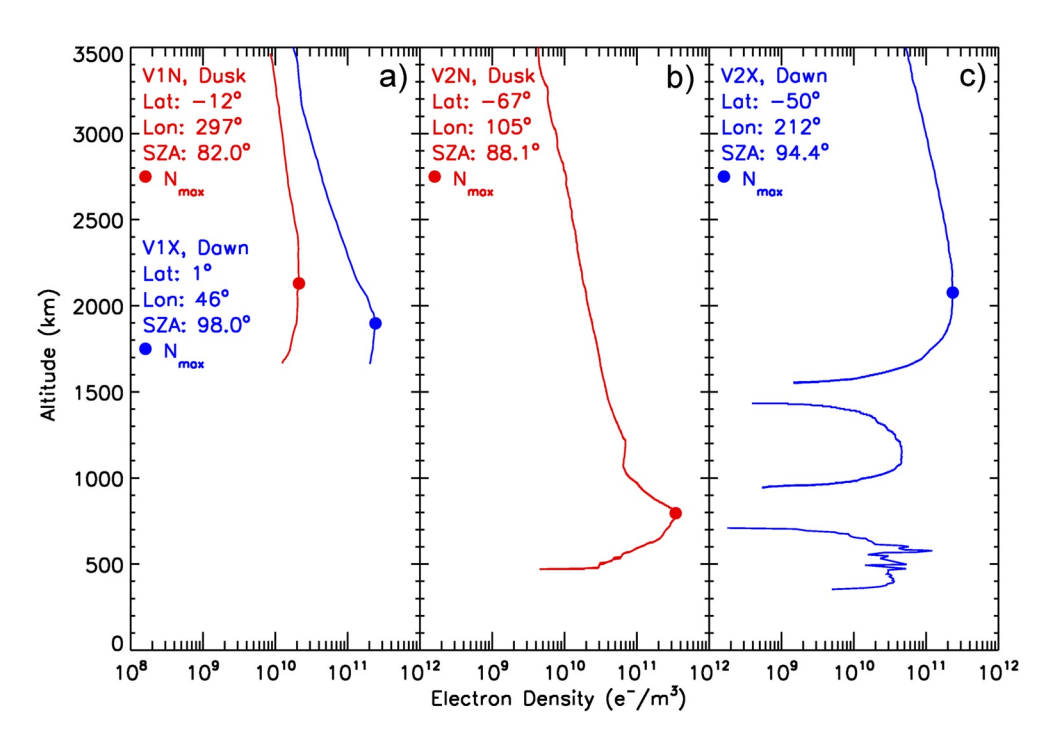


Figure 2. Ionospheric electron density profiles obtained from the Voyager-1 and -2 radio occultation experiment at Jupiter (Eshleman et al., 1979; Hinson et al., 1998) using the same format as in Figure 1. Longitudes are given in Table 1. Panel (a) incomplete profiles from Voyager-1. Panels (b and c) Profiles from Voyager-2. Dots are used to indicate N_{max} at h_{max} . For altitudes with data gaps, where retrieval yields negative electron density values, total electron content is calculated by interpolating the positive values above and below. Using zero values within data gaps has a minimal effect since the interpolated values are a few orders of magnitude lower than the positive values shown.

Numerically, the largest value of electron density $(23.3 \times 10^{10} \text{ e}^-/\text{m}^3)$ occurs at 2,077 km. This Voyager-2 N_{max} value at dawn is less than at dusk, as would occur for PCE conditions. For TEC, the Voyager-2 value at dawn (30 TECU) is the largest ever observed—and twice the value at dusk. If the V1X (dawn) profile did not have missing values at lower altitudes, it would yield a very high TEC value, perhaps above the 30 TECU found for V2X. Thus, for the three available pairs of occultations with complete $N_e(h)$ profiles (P10,V1, V2), the TEC values at dawn are greater than the TEC magnitudes at dusk. Once again, these are not ionospheric characteristics simply related to basic PCE conditions over the course of a day.

3.5. Quantitative Assessments of Pioneer and Voyager Profiles

The initial attempts to compare Pioneer and Voyager observations with models of the Jovian ionosphere all pointed out that the altitude range of maximum photo-ionization occurred between 500 and 1,000 km, well below the heights where $N_{\rm max}$ values were observed (e.g., see Figures 3–5 in McConnell et al. [1982]). To explore the extent that PCE mechanisms can account for observed patterns, we present in Figure 3 the following plasma parameters: (a) the maximum electron density, $N_{\rm max}$, (b) the average electron density within the PCE domain below 1,000 km (designated $\overline{[N_e]}_{<1,000\,{\rm km}}$) and (c) TEC—all adjusted to their values at 5.2 AU. Note that the maximum possible number of data points is seven—three from Pioneer and four from Voyager. Of these, only three were obtained with SZA <90° (see Table 1). All three were for "Dusk" conditions, with the V1N profile limited to high altitudes. Thus, only two profiles (P10N, V2N) can be used with Equation 5 with solar illumination conditions of SZA = 82° and 88°. The results for $N_{\rm max}$ appear as the solid line in Figure 3a. They are completely inconsistent (CC = -1.00) with the PCE Equation 5. Adding the V1N partial profile's $N_{\rm max}$ value does not improve the correlation (CC = -0.99), as shown by the dashed line.

Given the small range of SZAs, and their high values, there is little reason to focus on diurnal patterns portrayed by SZA values (or grazing incidence angle portrayals of SZAs). We thus looked for correlations of plasma

MENDILLO ET AL. 9 of 25

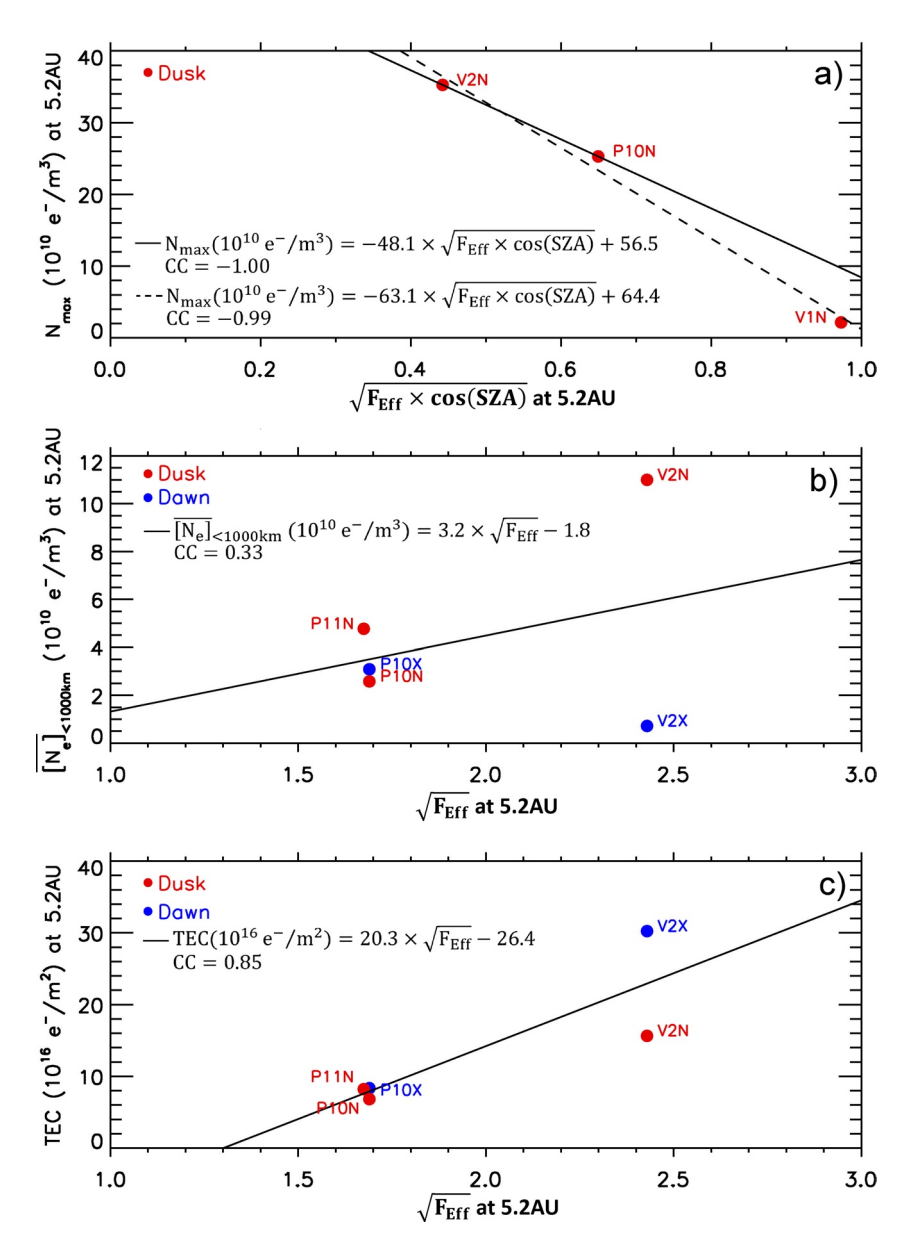


Figure 3. Photo-chemical-equilibrium (PCE) correlation results using the five complete $N_e(h)$ profiles from Pioneer and Voyager. (a) N_{max} versus the PCE factor defined in Equation 5 for the cases when solar zenith angle <90°. The dashed line is for all three values, while the solid line excluded the Voyager-1 value due to its incomplete $N_e(h)$ profile. (b) The average electron density below 1,000 km $(\overline{|N_e|}_{-1,000 \text{ km}})$ versus the square root of the effective solar flux index defined by Equation 3. (c) Total electron content versus the square root of the effective solar flux index defined by Equation 3.

parameters with the first PCE term in Equation 4, that is, the square root of the solar irradiance proxy index $(F_{\rm eff})$. The average electron density below 1,000 km $(\overline{|N_e|}_{<1,000~\rm km})$ is shown in Figure 3b. A pattern with solar flux emerges—the first indication of a correlation between observed electron densities and solar fluxes at Jupiter. Yet, with a CC of only 0.33, hardly a convincing finding. Moreover, the correlation is driven by a single high value from V2N. More promising are the results for TEC shown in Figure 3c. With TEC from V1N and V1X not used due to incomplete altitude coverage, the remaining data points offer a stronger correlation pattern (CC = 0.85). Thus, we characterize the yield from the Pioneer and Voyager data sets as inconclusive for diurnal or spatial effects characterized by SZAs, and in particular for $N_{\rm max}$, but informative for ionospheric TEC over longer time spans, that is, solar minimum to solar maximum.

MENDILLO ET AL. 10 of 25

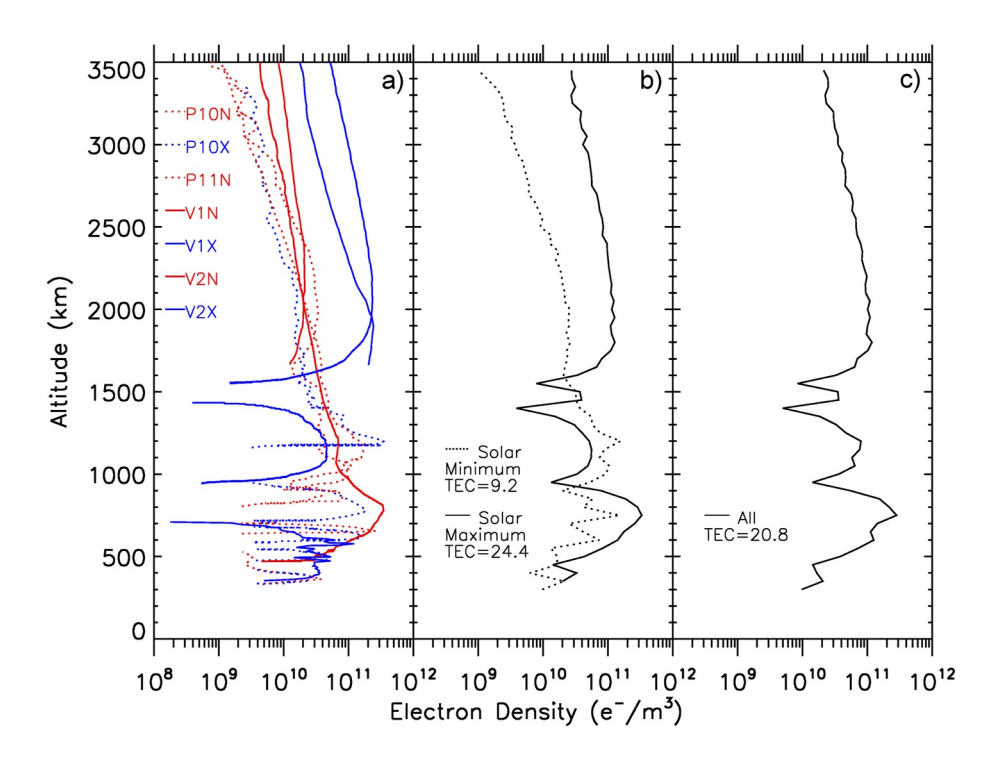


Figure 4. (a) Summary of the seven electron density profiles from the Pioneer and Voyager radio occultation experiments at Jupiter. The dotted lines refer to solar minimum conditions sampled by Pioneer-10 and 11, and the solid lines to the Voyager-1 and -2 results during solar maximum years (see Table 1). (b) Average of solar minimum profiles (dotted line) and solar maximum profiles (solid line). (c) Average of all profiles shown in panel (a). Total electron content values in panels (b and c) are in units of 10^{16} e⁻/m². The total electron content calculated for each profile is shown in Table 1.

The fundamental message to come from our analyses above can be assessed visually in Figure 4. Here we overplot the full set of Pioneer + Voyager profiles, with red showing dawn, blue showing dusk, and the dotted and solid lines showing solar minimum versus solar maximum conditions, respectively. In spite of the two partial profiles, and others having significant structures at lower heights, there is a clear solar cycle trend seen between the dotted and solid line portrayals of the profiles. The preponderance of solid lines occurs on the right side of the figure—these are the solar maximum profiles. Panel (b) shows the average profiles from Pioneer (dotted line) and Voyager (solid line). A clear trend appears in the topside ionosphere with a larger plasma scale height at solar maximum versus solar minimum—indicative of higher plasma temperature $(T_p = T_a + T_c)$ effects (see Section 5.5 in Schunk and Nagy [2009]). There is a less clear solar cycle trend at lower altitudes. Yet, the solar maximum N_a values are higher in the PCE domain below ~750 km. The TEC average values add strong quantitative evidence of a solar cycle effect (9 vs. 24 TECU). Collectively, these patterns account for the high correlation between TEC and solar flux. Finally, panel (c) gives the overall message from the combined Pioneer and Voyager missions. There are three height regimes of interest in the Jovian ionosphere: a high altitude region between $\sim 1,700$ and 2,000 km, an intermediate peak near ~1,200 km, and a bottom-side maximum near ~700 km. Using the terminology introduced in Figure 1, these three domains correspond approximately to the L1, L3, and L5 layers. In Section 7 below, we propose calling these the J3, J2, and J1 layers.

Before moving on to the Galileo radio occultation data sets, we want to document the simultaneous effects of changing solar cycle conditions upon ionospheres within the inner and outer solar system.

3.6. Results Using "Same Day" Ionospheric Data at Earth

The identification of the "rotated-Sun date" for use in Equations 4 and 5 has the additional advantage of enabling a companion analysis of PCE layers in the terrestrial ionosphere under the same solar conditions. This approach addresses the question if the few days of observations at Jupiter happened to be unusual periods of solar behavior—a question easily answered using terrestrial observations. This "comparative ionospheres" validation

MENDILLO ET AL. 11 of 25



Table 2
Earth Ionosonde Station Characteristics

Zurin Teriogorius Granieri Graniere									
Station		Chilton/Slough	Grahamstown						
Latitude		51.5	-33.3						
Longitude		0.6°W	26.5°E						
Midday SZA (°)	13 December 1973	75.4	14.5						
	9 December 1974	75.5	14.8						
	8 March 1979	57.5	30.9						
	20 July 1979	32.3	55.5						

exercise was used successfully in our earlier study of Saturn's ionosphere (Mendillo et al., 2018).

Values of the electron density observed in the F1-layer (EUV production) and the E-layer (soft X-ray production) are available from a global network of radar-sounding instruments ("ionosondes"). In our studies of "same day" ionospheres for Saturn and Earth, we identified several ionosonde locations with a good record of reliable observations. Guided by that study, Table 2 gives two terrestrial ionosonde locations (Chilton, UK; Grahamstown, South Africa) with data archives extending back to the Pioneer and Voyager radio occultation data sets in the 1970s. Note that the ranges of SZAs at mid-day are greater than the near-terminator SZAs from ROX experiments, and thus lend themselves to a more robust assessment of PCE processes portrayed by Equation 5.

Given the abundance and continuity of ionosonde observations, we decided to increase statistical confidence by using 3 days of ionosonde data corresponding to the rotated-Sun date, plus-and-minus a day. Moreover, as done with our previous Saturn-Earth comparisons, to maximize the reliability of data to be used, we selected "midday"

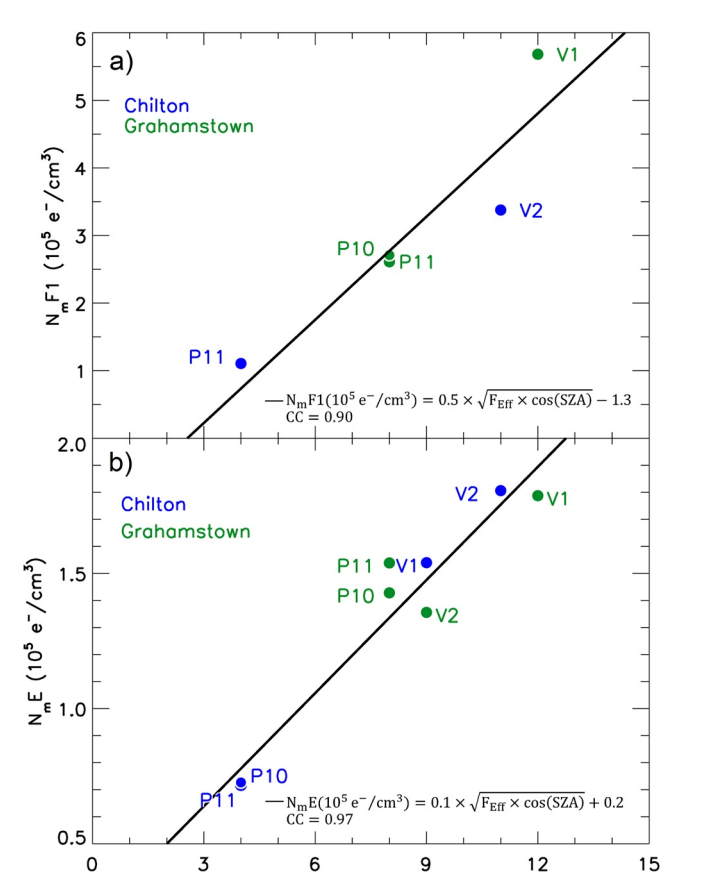


Figure 5. Comparison of "same day" ionospheric behavior at Earth for the photo-chemical-equilibrium layers of the E- and F1-regions of the terrestrial ionosphere. Note that the F1-layer data for the Pioneer 10 and 11 dates have overlapping points for Grahamstown in panel (a) and that the E-layer from Chilton have overlapping data points in panel (b). However, three data points are missing on panel (a), P10, V1, and V2, since measurements for these dates were not available.

 $\sqrt{\mathbf{F}_{\rm Eff}} \times \cos(\mathbf{SZA})$

values defined as the average of the hourly values obtained at 11-12-13 local times. In this way, the total of four calendar days of observations at Jupiter (see Table 1) are compared with up to twelve "same-Sun" days at Earth. This is preferable to using E- and F1-layer electron densities with SZAs near 90° because ionosonde methods are particularly uncertain for such conditions.

Figure 5 gives the PCE "same day" patterns at Earth for both the F1-layer (a) and the E-layer (b), using the terrestrial version of Equation 5. The statistical correlations are 0.90 and 0.97. Our conclusion is that on the days of ROX measurements at Jupiter by the Pioneer and Voyager spacecraft, the solar irradiance patterns occurring at Earth produced well-behaved ionospheric layers caused by PCE processes. Thus, we have no concerns about the Jovian observations occurring on unusual days in 1973, 1974, and 1979.

4. The Galileo Mission's Radio Occultation Profiles

The Galileo radio occultation experimenter (Dr. A. J. Kliore, now deceased) generated a set of images showing the 25 electron density profiles, which he provided to his colleague, Dr. D. P. Hinson, who recently supplied them to us. The first two profiles obtained on 8 December 1995 were described by Hinson et al. (1997). As with some of the Pioneer and Voyager observations, both of the initial $N_e(h)$ profiles from Galileo were highly structured at heights below 1,000 km. Hinson et al. (1997) suggested that the cause(s) of such structuring could be either atmospheric gravity wave effects or multi-path propagation issues. At higher altitudes, the $N_{\rm max}$ at ingress (dusk, red) was $10^{11} \, {\rm e^-/m^3}$ near 900 km—5 times the maximum electron density observed at egress (dawn, blue) at \sim 2,000 km. Hinson et al. (1997) discussed at length the non-PCE aspects of both profiles, suggesting that strong particle precipitation appears to be a dominant source of plasma within the Jovian ionosphere.

Only five of the Galileo profiles have been published—the first two in Hinson et al. (1997) and the others in Yelle and Miller (2004). These five profiles can be found at the Planetary Plasma Interactions Node of the Planetary Data System (Galileo Orbiter Jup/Io RSS Ionosph Ele Dens Profile Data, https://doi.org/10.17189/1519685). We created digital versions of the additional 20 profiles located at JPL. The generated data set can now be found at this site (https://hdl.handle.net/2144/43832). Figure 6 shows all 25 of the Galileo

MENDILLO ET AL. 12 of 25

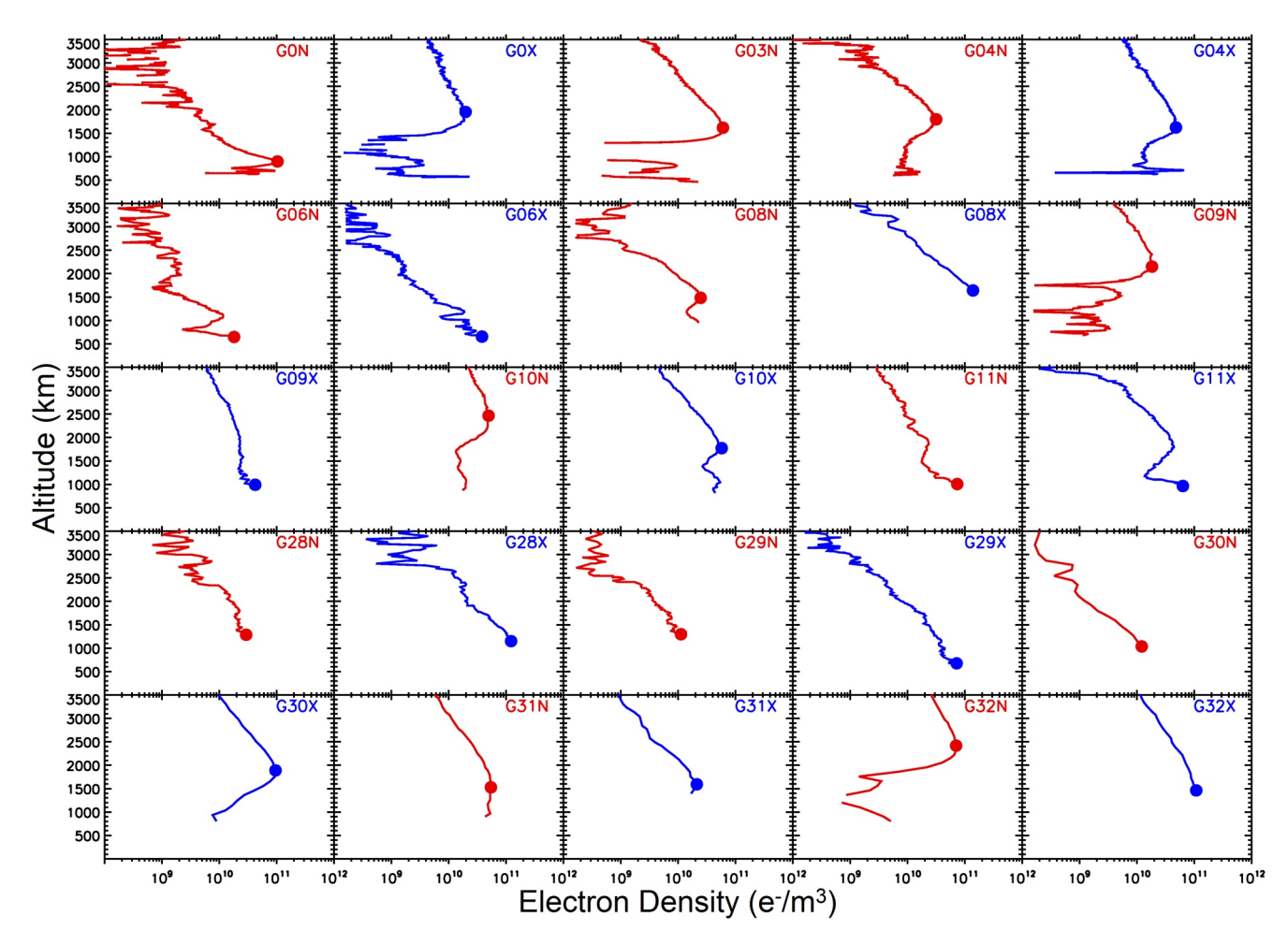


Figure 6. Electron density profiles of each Galileo radio occultation. Dusk profiles are displayed in red while dawn profiles are depicted in blue. The N_{max} values are marked with a dot in each occultation. See Table 3 for complete information about each occultation. See supporting information for full profiles, including a larger height range where available. These profiles can also be found at this site (https://hdl.handle.net/2144/43832).

electron density versus height patterns. The associated parameters for these profiles are summarized in Table 3 using the same format as for Pioneer and Voyager in Table 1. In Figure 6, we use a solid dot to show $N_{\rm max}$ for each profile; they span a decade of magnitudes—from $\sim 10^{10}$ e⁻/m³ at $\sim 1,300$ km (G29N) to $\sim 10^{11}$ e/m³ at ~ 900 km (G0N). There are profiles with monotonically increasing densities from 3,500 km down to ~ 500 km (e.g., G06X, G29X), profiles with high altitude (>1,500 km) peak densities (e.g., G03N, G04N, G09N, and G32N), and profiles with bottom-side layers (e.g., G0N, G0X, and G09N). While the highly structured bottom-side layers are of strong scientific interest, they are actually a minority characteristic of the overall Galileo data set.

To search for patterns, we show in Figure 7 the same profiles separated by solar flux conditions at 1 AU—solar minimum (F10.7 = 70–96) versus solar maximum (F10.7 = 161–200). Four categories are depicted: (a) Dawn at solar minimum, (b) Dusk at solar minimum, (c) Dawn at solar maximum, and (d) Dusk at solar maximum. There are several features to note. First, the high degree of variability found during the Pioneer and Voyager missions is confirmed by the Galileo observations. The solar minimum profiles (panels a and b) have excellent coverage in the PCE domain below 1,000 km (indicated by the dashed lines). For profiles obtained during the solar maximum years (bottom panels), there is essentially no coverage below 1,000 km. Such a data gap could be due to scientifically interesting effects, for example, highly disturbed ionospheric conditions during solar maximum years. Alternately, the low altitude data could be lost due to problems with the radio system linking the Galileo spacecraft to the Deep Space Network. Galileo's solar maximum observations occurred toward the end of the mission after the spacecraft had accumulated significant radiation damage. As will be shown below, the loss of

MENDILLO ET AL. 13 of 25



Table 3Galileo Radio Occultations Characteristics as Measured at Jupiter

								Electron density 10 ¹⁰ (e ⁻ /m ³)			TEC°
Occultation	Date	Rotated-Sun date	Lat (°)a	Lon (°)a	SZA (°)	Jupiter-Sun distance (AU)	Rotated flux effective (1AU)	$N_{ m max}$	$\overline{[N_e]}$ <1,000 km	Height $(km)^b$ of N_{max}	10^{16} (e ⁻ /m ²)
G0N, Duske	8 December 1995	21 December 1995	-24	292	88.6	5.3	69.6	10.3	6.0	896	3.7
G0X, Dawn ^e	8 December 1995	21 December 1995	-43	332	91	5.3	69.6	2.0	0.3	1,954	2.3
G03N, Duske	November 8 1996	16 November 1996	-28	102	82.2	5.2	72.3	6.0	0.5	1,617	5.6
G04N, Duske	21 December 1996	1 January 1997	-23	246	86.3	5.1	72.6	3.2	0.9	1,795	3.4
G04X, Dawne	22 December 1996	3 January 1997	-25	167	93.8	5.1	73.0	4.8	1.7	1,622	6.5
G06N, Duskf	26 February 1997	15 February 1997	-4	195	95.5	5.1	71.1	1.8	0.7	647	0.8
G06X, Dawn ^f	27 February 1997	16 February 1997	-4	234	84.4	5.1	71.2	3.8	2.4	655	1.6
G08N, Duskf	25 May 1997	20 May 1997	-33	285	99	5.1	78.0	2.5g		1,483	2.2
G08X, Dawnf	26 May 1997	21 May 1997	-27	132	79.9	5.1	80.8	13.9g		1,640	6.0
G09N, Duskf	1 August 1997	31 July 1997	-1	90	91.7	5.1	76.6	1.8	0.2	2,149	2.2
G09X, Dawn ^f	2 August 1997	2 August 1997	-1	60	88.5	5.1	76.7	4.2 ^g		990	4.5
G10N, Duskf	29 September 1997	2 October 1997	12	56	81	5.0	88.6	5.0g		2,466	7.7
G10X, Dawn ^f	30 September 1997	3 October 1997	16	330	98.9	5.0	87.4	5.8	4.4	1,772	7.9
G11N, Duskf	16 November 1997	23 November 1997	18	20	79.3	5.0	95.5	7.4 ^g		1,005	4.1
G11X, Dawn ^f	16 November 1997	23 November 1997	24	352	99.9	5.0	95.5	6.3 ^g		964	5.2
G28N, Duskf	20 May 2000	7 May 2000	76	191	90.7	5.0	160.9	2.9g		1,286	2.3
G28X, Dawn ^f	20 May 2000	7 May 2000	72	280	89.7	5.0	160.9	12.2 ^g		1,150	6.8
G29N, Duskf	28 December 2000	30 December 2000	68	179	88.2	5.0	171.7	1.1 ^g		1,297	0.6
G29X, Dawn ^f	28 December 2000	30 December 2000	70	281	92.6	5.0	171.7	7.2	4.8	675	4.3
G30N, Duskf	23 May 2001	4 June 2001	31	262	87.4	5.1	160.0	1.2 ^g		1,036	0.6
G30X, Dawn ^f	23 May 2001	4 June 2001	31	344	92.9	5.1	160.0	9.6 ^g		1,889	11.1
G31N, Duskf	5 August 2001	26 July 2001	12	303	97	5.1	144.0	5.4 ^g		1,528	8.4
G31X, Dawn ^f	6 August 2001	27 July 2001	15	47	83.2	5.1	143.0	2.1 ^g		1,593	1.7
G32N, Duskf	15 October 2001	10 October 2001	20	190	100.4	5.1	199.5	7.0 ^g		2,418	8.0
G32X, Dawn ^f	15 October 2001	10 October 2001	21	303	79.7	5.1	199.5	10.8g		1,462	10.0

^aLatitudes and longitudes are in System III, 1965.0. ^bAll heights are referenced to the 1 bar level. ^cTEC was integrated from the bottom of the profile up to 3,500 km and thus with different column extents. For altitudes with data gaps, where retrieval yields negative electron density values, TEC is calculated by interpolating the positive values above and below. Alternatively, zero values for electron could have been assumed, the resulting TEC would differ by a very small amount, an average of 0.004 TEC units. ^dAverage electron density below 1,000 km, calculated whenever the profile extends down to at least 850 km and five or more values are available for averaging. ^ePDS: https://doi.org/10.17189/1519685. ^fFrom Dr. A. J. Kliore through Dr. D. P. Hinson. ^eN_{max} values shown are only for information purposes—not included in analyses due to lack of data at low heights.

low altitude data prevents attempts to confirm the solar cycle effects found in comparisons of the Pioneer (SMIN) and Voyager (SMAX) height-integrated parameters (TEC and $\overline{[N_e]}_{< 1.000 \text{ km}}$), as shown in Figures 3a and 3b.

In Figure 8 we show the averages of solar minimum profiles at dawn and dusk in panel (a), together with the averages of solar maximum profiles in panel (b). Panel (c) combines dawn and dusk profiles to show overall solar cycle effects. Most striking is the agreement in topside ionosphere patterns at heights above \sim 1,500 km. This lack of a solar cycle effect in the topside ionosphere is in marked contrast to the Pioneer-Voyager patterns shown in Figure 4. Yet, at heights below \sim 1,500 km, the effect of solar cycle is clearly apparent in the Galileo data. The TEC values (in units of 10^{16} e⁻/m²) shown in each panel portray the overall effect of changing solar cycle conditions. The average profile from the Galileo mission shown in panel (d)—averaging over all locations, dawn/dusk times and solar cycle conditions—has approximately the same morphology as the overall average patterns from

MENDILLO ET AL. 14 of 25

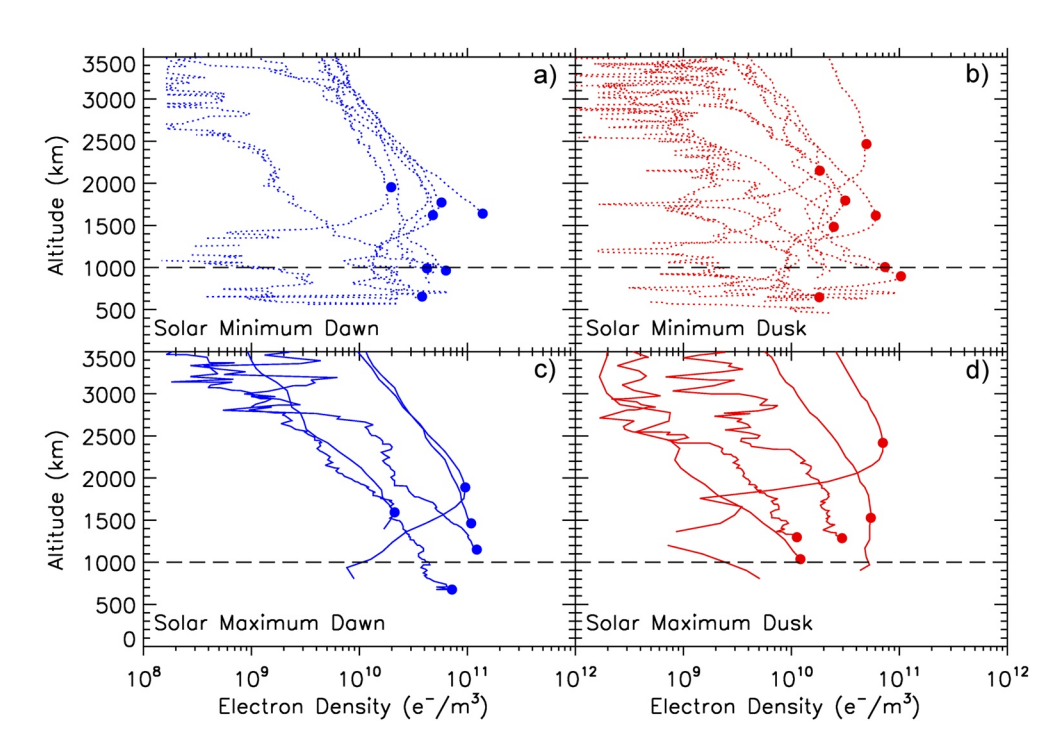


Figure 7. Summary of the electron density profiles obtained by the radio science experiment on the Galileo satellite mission to Jupiter: (a) Dawn at: solar minimum, (b) Dusk at solar minimum, (c) Dawn at solar maximum, and (d) Dusk at solar maximum. In each profile, a solid dot is used to identify the maximum electron density (N_{max}) value. A dashed line at 1,000 km is used to indicate the approximate top of the photo-chemical-equilibrium domain.

Pioneer and Voyager shown in panel (c) of Figure 4. Yet, the electron density and TEC values are considerably different. Using Figure 1 terminology introduced by Fjeldbo et al. (1975) and Woo and Yang (1978), the three average layers from Galileo approximate the L1, L3, and L5 layers depicted in Figure 4c from the Pioneer and Voyager era.

5. Combined Data Sets

The distributions of characteristic features of the total data set (Pioneer + Voyager + Galileo) appear in histogram forms Figure 9: (a) solar zenith angles, (b) the rotated-Sun solar flux parameter ($F_{\rm eff}$, see Equation 3) at 1 AU, (c) maximum electron density ($N_{\rm max}$), (d) height ($h_{\rm max}$) of $N_{\rm max}$, (e) mean density below 1,000 km, $\overline{[N_e]}_{<1,000\,{\rm km}}$, and (f) TEC of observed $N_e(h)$ profiles.

The SZA pattern in panel (a) is typical of outer-planet radio occultation experiments where data sets are confined within $\sim \pm 15^{\circ}$ of terminator conditions. There are approximately equal numbers of profiles with SZAs above and below 90°. Panel (b) shows that the small number of solar-min versus solar-max profiles from Pioneer and Voyager are now enhanced by the larger set from Galileo. Panel (c) shows the confusing pattern of Pioneer's solar minimum data having some of the highest peak electron density values. Panel (d) shows that the h_{max} values are highly variable. Panels (e and f) show that the distributions of height-integrated parameters differ during the Galileo era from the previous Pioneer-Voyager periods.

Perhaps the most striking aspect of comparisons between Galileo data and the earlier Pioneer and Voyager observations is the fact that the solar maximum value of average TEC from Galileo (6.2 TEC units, TECU) is much lower than the average TEC found with Voyager (24.4 TECU). A comparison of the solar minimum average TEC values is also different: 9.2 TECU for the Pioneer era in comparison to 4.8 TECU for Galileo's solar minimum data.

Figure 10 shows the overall characteristics of the three solar cycles of relevance from the Pioneer to Galileo eras. The F10.7 solar radio flux values at 1 AU show the solar minimum period during the early 1970s to be somewhat more variable than the deep solar minimum years of the 1990s. Yet, for Pioneer $< F10.7 > _{1 \text{ AU}} = 77$ units, while

MENDILLO ET AL. 15 of 25

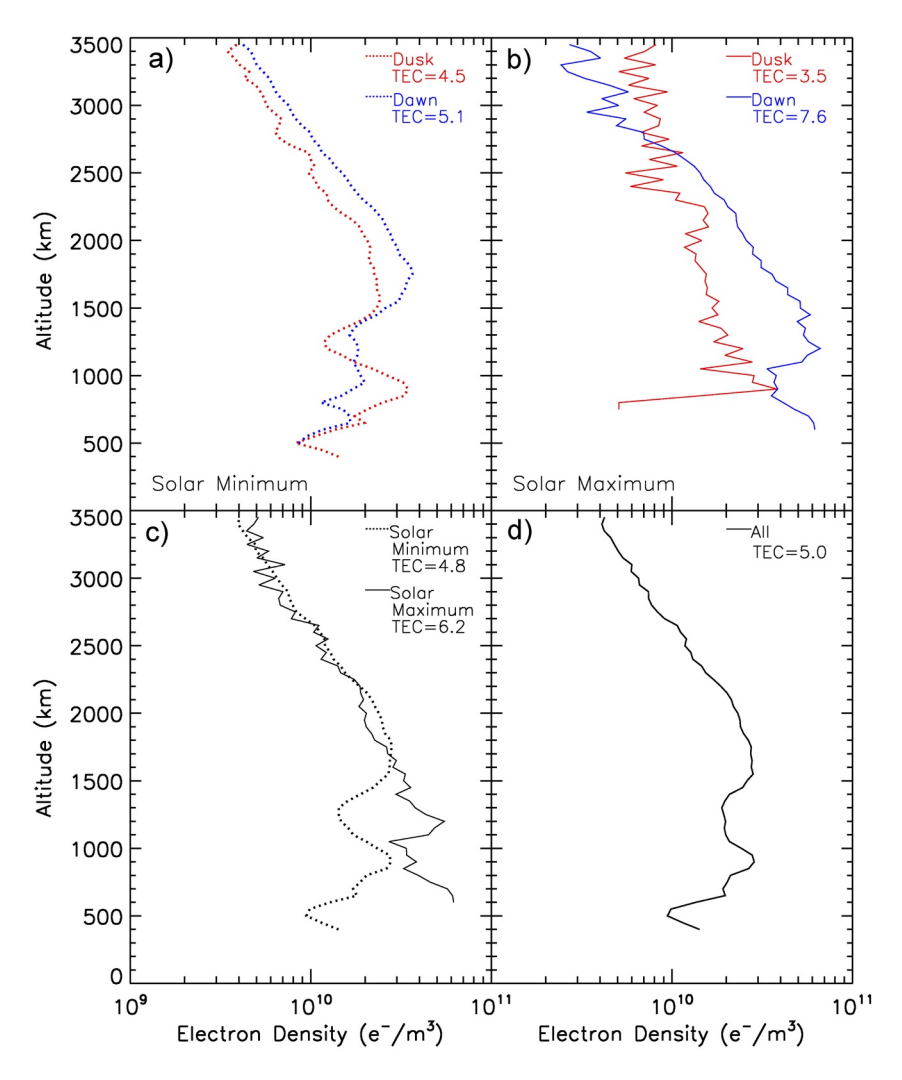


Figure 8. (a) Red and blue dotted curves show average Galileo dusk and dawn profiles during solar minimum. (b) The red and blue solid lines show the average dusk and dawn profiles during solar maximum years. (c) Comparison of average solar maximum profiles (dotted line) and solar minimum profiles (solid line), (d) Average of all Galileo profiles. TEC values are in units of 10^{16} e⁻/m². All averages are calculated with a 50 km resolution. Note that all have been smoothed with a running 3-point average to better show the trends.

for the Galileo solar minimum data $<F10.7>_{1~{\rm AU}}$ was nearly identical (79 units). The Voyager era occurred during the rising phase of a strong solar cycle, with its $N_e(h)$ profiles having $<F10.7>_{1~{\rm AU}}=172$ units. The Galileo data at solar maximum occurred during a more quiescent solar cycle, but their $<F10.7>_{1~{\rm AU}}$ average value of 167 units hardly differentiates the two eras. Using those average F10.7 values to characterize production by solar irradiance would suggest essentially identical ionospheres from Pioneer/Voyager to Galileo.

The three dominant layers shown in Figures 4c and 8d offer testimony to that consistency. Yet the magnitudes of the electron densities of those layers differ, and the TEC values show solar-max versus solar-min values that are quite different. This again suggests that a non-solar photon source of ionization (e.g., particle precipitation) could have played a different role during each era.

6. Analysis of Galileo Data and Comparisons With Pioneer and Voyager

6.1. Magnitudes of Maximum Electron Density and TEC

Data analysis using Equation 5 suffers from the very small range in solar zenith angles possible for radio occultation experiments for outer planets. Nevertheless, there are 13 profiles in Table 3 that have SZA <90°. The results

MENDILLO ET AL. 16 of 25

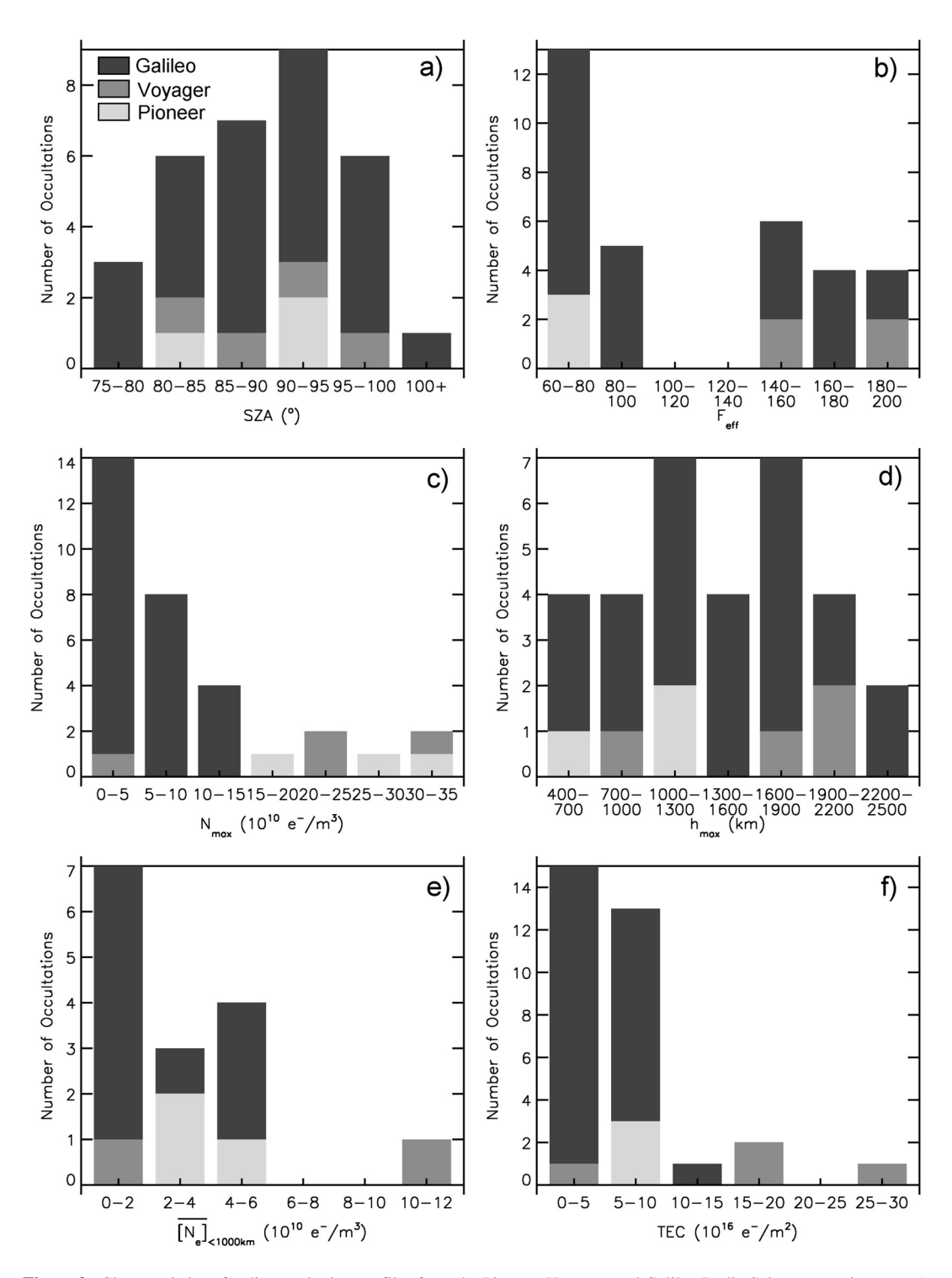


Figure 9. Characteristics of radio occultation profiles from the Pioneer, Voyager, and Galileo Radio Science experiments: (a) Solar Zenith Angles, (b) the rotated-Sun solar flux parameter ($F_{\rm eff}$) at 1 AU, (c) maximum electron density ($N_{\rm max}$), (d) height of $N_{\rm max}$, (e) $\overline{[N_e]}_{<1,000~{\rm km}}$ and (f) observed total electron content.

of using their N_{max} values with Equation 5 appear in Figure 11a. With a CC of 0.1, there is no statistically significant pattern of Galileo maximum electron densities with PCE processes. For the $\overline{[N_e]}_{<1,000 \text{ km}}$ parameter and TEC, incomplete profile coverage at lower heights during solar maximum years (see Figures 7c and 7d) negates

MENDILLO ET AL. 17 of 25

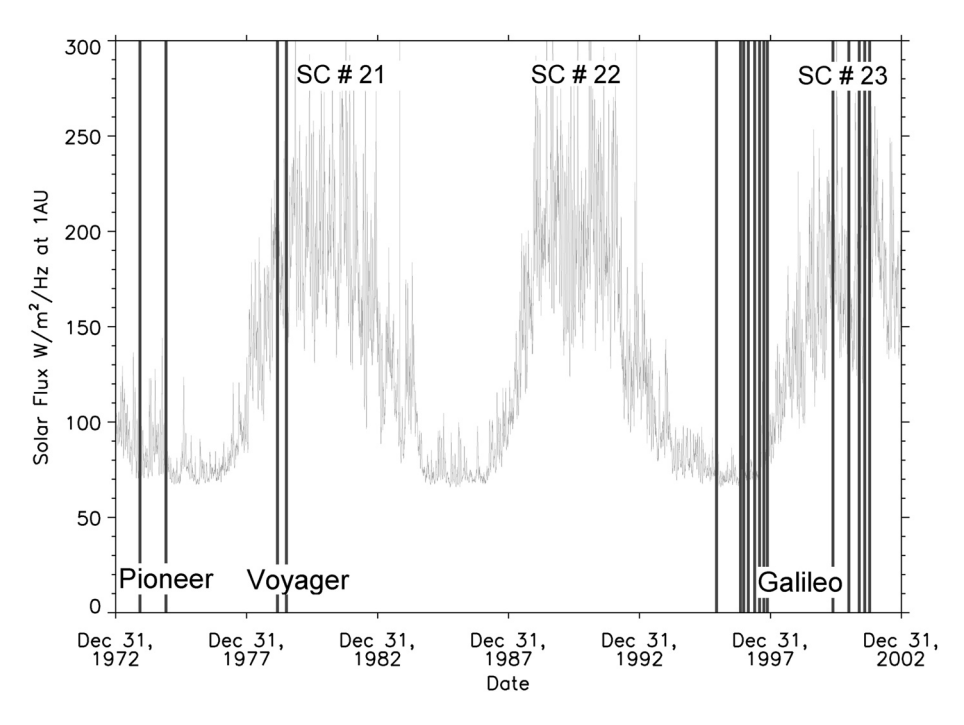


Figure 10. Solar Flux patterns (at 1 AU) spanning three solar cycles. The vertical lines indicate the times when radio occultation observations were made during the Pioneer encounters at Jupiter (solar cycle #20 minimum), the Voyager encounters (solar cycle #21 maximum), and the Galileo mission encounters during solar cycle #22 minimum and cycle #23 maximum.

any attempt to document solar cycle patterns. Galileo's profile G29X is, in fact, the only one to have full altitude coverage under solar maximum conditions.

The statistical results for TEC from Pioneer and Voyager shown in Figure 3 came from examining only the solar flux parameter ($F_{\rm eff}$). Applying that approach to the Galileo observations yields the patterns shown in Figure 11b. As can be seen, there is a positive CC of 0.6 for the Galileo data. This is less than the CC = 0.85 in Figure 3. Nevertheless, we conclude that the TEC parameter is a better indicator than $N_{\rm max}$ values for solar cycle changes of Jupiter's ionosphere. Recall from Figure 1d that the TEC contribution functions show that nearly 50% of the TEC comes from heights within the PCE dominant altitude range.

6.2. Spatial Patterns

In the preceding sections, we have concentrated exclusively on a solar photon produced ionosphere at Jupiter. To assess the observational evidence for auroral sources, we show in Figure 12a the distribution in latitude and longitude of radio occultation $N_e(h)$ profiles from the three missions (Pioneer + Voyager + Galileo). Average equatorward boundaries of the auroral ovals in each hemisphere are shown, together with the "magnetically mapped" footprints of the moon Io (taken from Nichols et al. [2009] and Bonfond et al. [2017], respectively). There are four profiles from Galileo above 68° latitude (North)—G28N, G28X, G29N, G29X (shown in Figure 6), and two profiles from Pioneer-Voyager in the southern hemisphere above 67°—P11N, V2N shown in Figures 1c and 2b. We averaged these potentially "auroral profiles" to get the pattern shown in panel (b); the average of the remaining "sub-auroral" profiles appears in panel (c). The auroral morphology is one with a single peak near 700 km, while the sub-auroral average profile exhibits the three-layer pattern shown earlier. Note that the TEC at auroral latitudes is also higher than at sub-auroral latitudes. Modeling studies of a precipitation source of Jovian plasma are described by Cravens (1987), Waite and Cravens (1987), Maurellis and Cravens (2001), and Majeed et al. (2004). Figure 2 in Maurellis and Cravens, for example, shows strong electron impact production near 400 km for both H⁺ and H₂⁺. Finally, we conducted a preliminary search of auroral images taken by the Hubble Space Telescope and did not find a suitable case study to pursue, but more effort is needed on this topic.

MENDILLO ET AL. 18 of 25



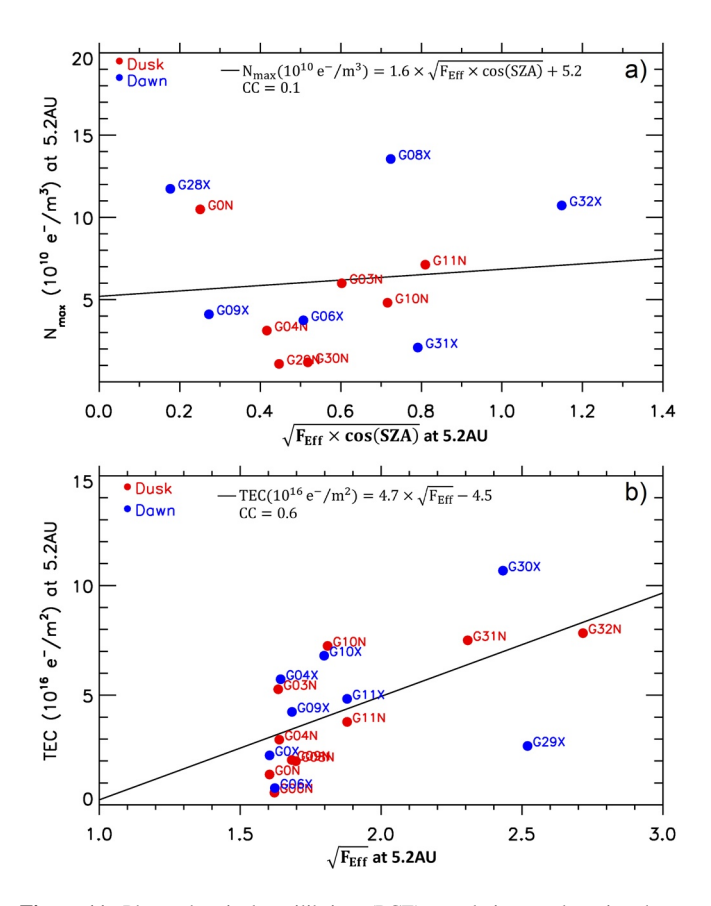


Figure 11. Photo-chemical-equilibrium (PCE) correlation results using the complete $N_e(h)$ profiles from Galileo. (a) $N_{\rm max}$ versus the PCE factor defined in Equation 1 for the 13 cases when solar zenith angle <90° (b) Total electron content between 1,000 and 3,500 km versus the square root of the effective solar flux index defined by Equation 3.

The spatial pattern of observational locations shown in the top panel of Figure 12 offers a sufficient global distribution to attempt longitude-averaged latitude patterns of observed parameters. Figure 13 shows such an analysis for maximum electron density $(N_{\rm max})$ in panel (a), the height of maximum density $(h_{\rm max})$ in panel (b), and TEC in panel (c). The red and blue dots show, as in previous figures, values from "dusk" and ("dawn") occultations. The large black dots give average values using broad 30° latitude bins. Consistent with patterns noted earlier, most of the blue dot (dawn) observations of $N_{\rm max}$ and TEC are larger than those for dusk (red) in panels (a and c). This is not the case for $h_{\rm max}$ values in panel (b). The latitude pattern for $N_{\rm max}$ and TEC show minimum values near the equator—portraying an "equatorial anomaly" type of effect long known for Earth (Rishbeth & Garriott, 1969; Schunk & Nagy, 2009). Mahajan (1981) was the first to note such a possibility at Jupiter. More recently, Stallard et al. (2018) noted that H_3^+ brightness patterns also reveal a "dark ribbon" along the jovigraphic equator.

7. Summary

7.1. Yield From Pioneer and Voyager Missions

We have re-examined the electron density profiles at Jupiter obtained by discovery-mode radio occultation experiments (ROX) conducted during the fly-bys of the Pioneer (1973) and Voyager (1979) missions. The observational conditions sampled correspond to solar minimum (Pioneer) and maximum (Voyager). Inherent in ROX data for outer planets, the local time coverage was constrained to near solar-terminator conditions: Ingress/dusk versus egress/dawn, with solar illumination varying with height. The $N_e(h)$ patterns obtained are summarized in Figure 4. They often (but not always) had highly structured variations with height, making it difficult to identify the maximum electron density ($N_{\rm max}$) and its height of occurrence ($h_{\rm max}$) in ways consistent with expectations from PCE theory, that is, at height domains without effects of plasma dynamics.

In a new approach, we examined height-integrated quantities in order to eliminate ambiguities that arise from highly variable structures with altitude. We

formed (a) TEC, defined as the integral of each profile with height and (b) the average electron density below 1,000 km ($\overline{[N_e]}_{<1,000 \text{ km}}$), shown by modeling to be fully within the PCE domain (see, e.g., Figure 3 in McConnell et al. [1982]). The TEC parameter provides a single number to characterize each profile and thus offers a way to compare Jupiter's overall ionosphere under different local time and solar cycle conditions. The $\overline{[N_e]}_{<1,000 \text{ km}}$ parameter provides a measure of mean plasma magnitudes associated only with basic photo-production balanced by chemical-loss.

We found that the paired (ingress/egress) TEC values of each mission had dawn sector values higher than at dusk for all data sets (see Table 1). This is inconsistent with diurnal patterns described by solar zenith angles controlling solar irradiance production of ion-electron pairs, followed by their chemical recombination. Our major finding appears in Figure 3c—showing a consistency for long-term patterns of TEC with solar flux changes over a solar cycle time span. A weaker correlation appeared for $\overline{[N_e]}_{< 1,000 \text{ km}}$ in Figure 3b.

Given the low number of $N_e(h)$ profiles from the Pioneer and Voyager missions, we conducted "same-day" analyses of patterns in PCE ionospheric layers at Earth. We found strong correlations with solar flux, indicating that the few days sampled by Pioneer and Voyager fly-bys were in no way unusual periods of solar-planetary processes in the solar system.

MENDILLO ET AL. 19 of 25



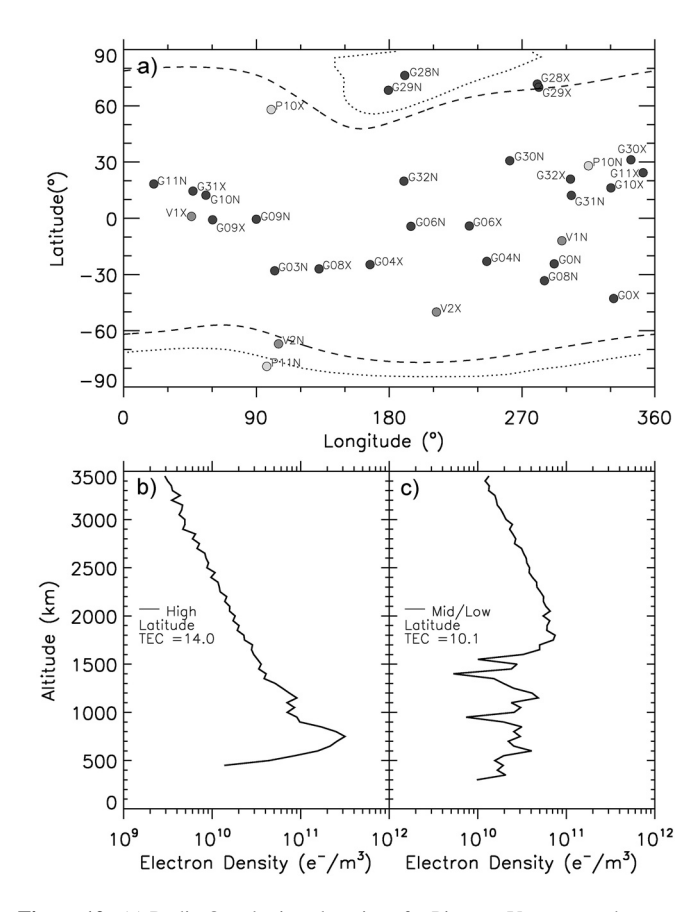


Figure 12. (a) Radio Occultations locations for Pioneer, Voyager, and Galileo electron density profiles. Pioneer locations are shown in light gray, Voyager are in gray, and Galileo's are shown in dark gray. Dotted lines indicate the main auroral ovals in the northern and southern hemisphere (Nichols et al., 2009). The dashed lines show the Io footprint for both hemispheres (Bonfond et al., 2017). (b) Average of the six electron density profiles measured at latitudes greater than 67° South and North. (c) Average of electron density profiles measured between 60°N and 60°S.

7.2. Yield From the Galileo Mission

The ROX experiments conducted by the Galileo radio science team had a yield of 25 profiles, more than three times the number from Pioneer + Voyager. As with the earlier data sets, Galileo sampled both solar cycle minimum and maximum conditions. Somewhat un-anticipated, the major science yield from the larger number of Galileo's ROX profiles was simply a basic confirmation of the same morphology patterns sampled sparsely in earlier decades. The Jovian ionosphere persists as a complex system. Perhaps our most significant finding was that the average of the seven profiles from Pioneer and Voyager data resulted in a three-layer plasma system (Figures 4a and 4b) nearly identical to the three-layer system documented by Galileo (Figures 8c and 8d). To offer an overall target for future modeling studies, we combined all data sets (32 profiles) to produce Figure 14. Using the terminology introduced by Rishbeth and Mendillo (2004) of numbering ionospheric layers from low to high altitudes, the three dominant regimes are displayed as the J1, J2, and J3 layers in Figure 14—approximately with local maxima at ~700, ~1,200, and ~1,700 km. Vertical integration of these profiles yields a solar cycle pattern for TEC values, with a factor greater than three from solar minimum (6.0 TECU) to solar maximum (20.5 TECU) values.

8. Future Work

8.1. Targets for Future Modeling

Our attempt to find the first approach to modeling Jupiter's ionosphere led us to a paper by Henry Rishbeth (1959). Using possible neutral atmospheres proposed by Kuiper (1952), ionospheric theory by Sydney Chapman (1931a, 1931b), and reaction rates by Bates and Massey (1946, 1947), estimates of maximum electron density values were in the $10^6 \, \mathrm{e^-/cm^3}$ range—now known to be a factor of 10 above observed values. As might be expected once space age observations became possible, advanced numerical models of the Jovian ionosphere appeared shortly after the Pioneer mission. They continued to evolve following the Voyager encounters, and most recently after the Galileo series of occultation experiments. A comprehensive, recent modeling treatment appears in Egert et al. (2017). To help focus discussion, we show in Figure 15 a representative set of profiles for the constituents of

the neutral atmosphere, together with ion and electron density profiles produced by photo-ionization and associated atmospheric chemistry (taken from Figure 7 in Moore et al. [2019]).

As shown in the left panel, molecular hydrogen (H_2) is the dominant neutral throughout most of Jupiter's ionosphere (h < 2,500 km). Yet, the main ions present are H^+ and H_3^+ (center panel). The former results from photo-ionizations of H and the dissociative ionization of H_2 . The H_3^+ ion is the result of subsequent chemistry (see Equations 6 and 7, above). As with Venus, Earth, Mars and Saturn, EUV photons produce the main layer, and soft X-rays produce the lower altitude layer. These appear in Figure 15a as the peak near 900 km and the lower altitude inflection point near 500 km. We associate the J1 and J2 layers with such PCE processes below $\sim 1,000 \text{ km}$. However, the observed profiles (Figures 4a and 6) deviate considerably from this simple picture, and particularly so when highly structured layers appear in the bottom-side ionosphere. That is, PCE processes can be so modified by local waves or meteoric ions that the photo-ionization layers are not observed as clear features.

Above the PCE domain ($h > \sim 1,000$ km), a topside layer we call J3 (typically near 1,700 km) varies from not apparent, as in G0N (first entry in Figures 6 and 15c), to the only layer observed (as V1N and V1X in Figure 2a). Figure 15b offers a possible answer. When the charge-exchange reaction due to H_2 ($v \ge 4$) facilitating conversion of atomic ions to molecular ions is not particularly strong, there is no topside "bite-out" near 1,500–1,700 km, and thus no J3 layer is evident. Conversely, if an enhanced abundance of H_2 ($v \ge 4$) is present, it removes more H^+ ions below $\sim 1,500$ km—thereby leading to a distinct J3 layer. This type of scenario (high vs. low impact of

MENDILLO ET AL. 20 of 25

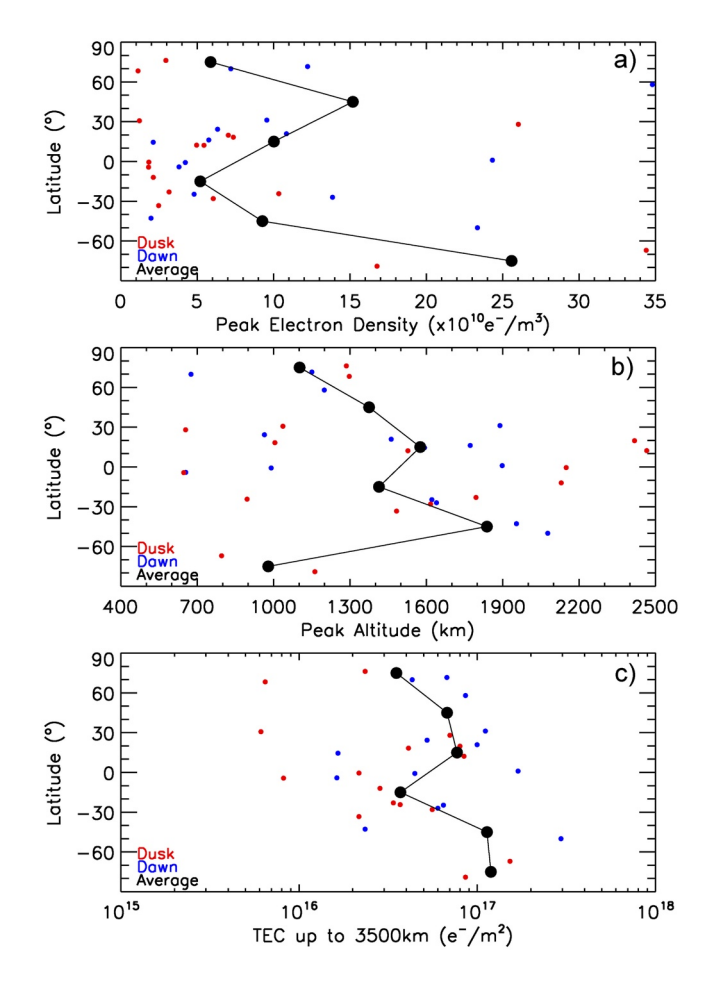


Figure 13. (a) Maximum electron density (N_{max}) , (b) the height of maximum density (h_{max}) and (c) total electron content measurements versus latitude. The red and blue dots show values from dusk and dawn occultations, respectively. The large black dots give average values using broad 30° latitude bins.

 ${\rm H_2}\,(v\geq 4))$ on plasma recombination was a possibility investigated by Majeed et al. (1999), as shown in their Figures 2 and 3 for the first two $N_e(h)$ profiles obtained by Galileo's ROX (Hinson et al., 1997; profiles GON and GOX in Figure 6 and Table 3). Clearly, additional modeling studies are needed to explore such scenarios. For example, several previous model studies have invoked neutral winds and plasma dynamics with specific magnitudes needed to modify results that come from photo-chemical-only simulations. Models with self-consistently derived magnitudes of neutral and plasma dynamics, together with effects due to energetic particle precipitation, are needed. For the latter, Figures 15b and 15c offer observational/validation goals for the Juno spacecraft's upcoming ROX experiments at high latitudes scheduled to start July 2023.

The much-awaited Juno ROX experiments should offer improvements over the $N_e(h)$ profiles obtained from the Galileo Mission that was forced to use the satellite's low-gain antenna. Juno will have a high gain antenna, thereby improving signal-to-noise. Moreover, it will use a higher frequency (Ka-band) to reduce the multi-path effects encountered by Galileo's S-band system. Lessons learned from Juno will also inform a future decision on whether or not it will be possible to reprocess the Galileo observations and, indeed, the possibly archived original telemetry from the Pioneer and Voyager missions.

8.2. Impact of H₃⁺ Observations

As reviewed by Miller et al. (2020), observations of H_3^+ have been remarkably useful for learning about giant planet upper atmospheres, especially at Jupiter. A majority of past H_3^+ observations focused on imaging the aurora, as those ever-shifting emissions yield insight into global magnetospheric dynamics (e.g., Mura et al., 2017). Spectroscopic observations additionally allow for derivation of H_3^+ temperatures and densities, enabling investigation of global upper-atmospheric energetics (e.g., O'Donoghue et al., 2021) and auroral currents (Dinelli et al., 2017; Gérard et al., 2020). The vast majority of past H_3^+ observations are vertically integrated, however, whereas a vertical number density profile would be the most useful comparison for the range of confusing patterns of $N_e(h)$ revealed by spacecraft radio occultations. Unfortunately, only a few prior limb observations exist (Lystrup et al., 2008; Migli-

orini et al., 2019; Uno et al., 2014), and none of them were obtained near in time to a radio occultation. Therefore, the Juno spacecraft's upcoming ROX experiments, scheduled to start July 2023, offer an enticing opportunity for simultaneous ground- or space-based H_3^+ limb profiles along with corresponding modeling.

8.3. Summary of Outstanding Issues

The results presented in this study identified several gaps in our understanding of the Jovian ionosphere. Some of these issues date to the very first radio occultation profiles obtained during the Pioneer missions of 1973–1974. Future investigations are needed in the following areas:

- 1. Can models reproduce a three-layer ionosphere and provide the reasons why all profiles observed are not triple-layered? (see Figure 14)
- 2. Can models explain why $N_e(h)$ profiles observed prior to dawn are often more robust (i.e., have higher electron densities) than occur at dusk on the same local time day? (see Figures 1, 2, and 8)
- 3. Can models explain why the parameter TEC offers more consistent patterns of PCE behavior than values of maximum electron density (N_{max}) ? (see Figure 11)
- 4. Can models explain why TEC at dawn is often higher than TEC at dusk?
- 5. What is the driving mechanism for the apparent "equatorial ionization anomaly" found in Jupiter's ionosphere? (see Figure 13)

MENDILLO ET AL. 21 of 25

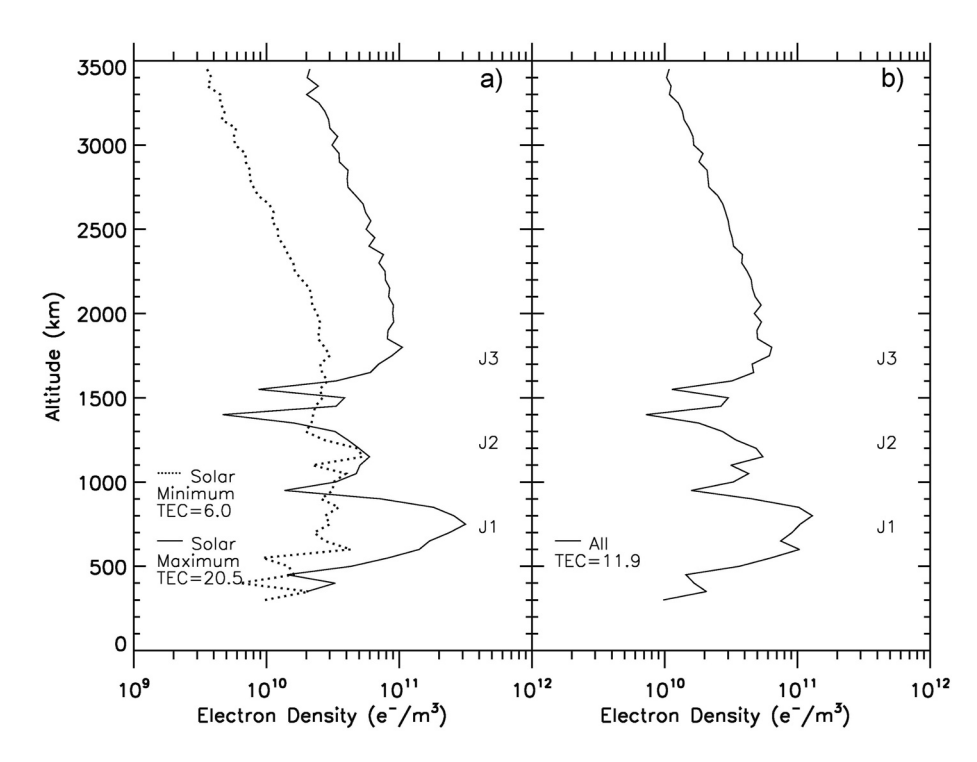


Figure 14. Assessing the combined data sets from Pioneer, Voyager and Galileo Radio Occultation Experiments. (a) Dotted curve represents the average of all solar minimum occultations, while the solid line depicts the average of all solar maximum occultations. (b) Average of all occultations. See text.

- 6. Why did the Jovian ionosphere show different N_{max} and TEC magnitudes during two relatively similar solar cycles? (see Figures 3, 8, and 11)
- 7. Can the auroral $N_e(h)$ profiles be reproduced in models using the same energetic particle precipitation parameters that account for auroral emissions? (see Figure 12)
- 8. Can lessons learned from upcoming Juno radio occultations provide insights on improvements to data analysis methods?

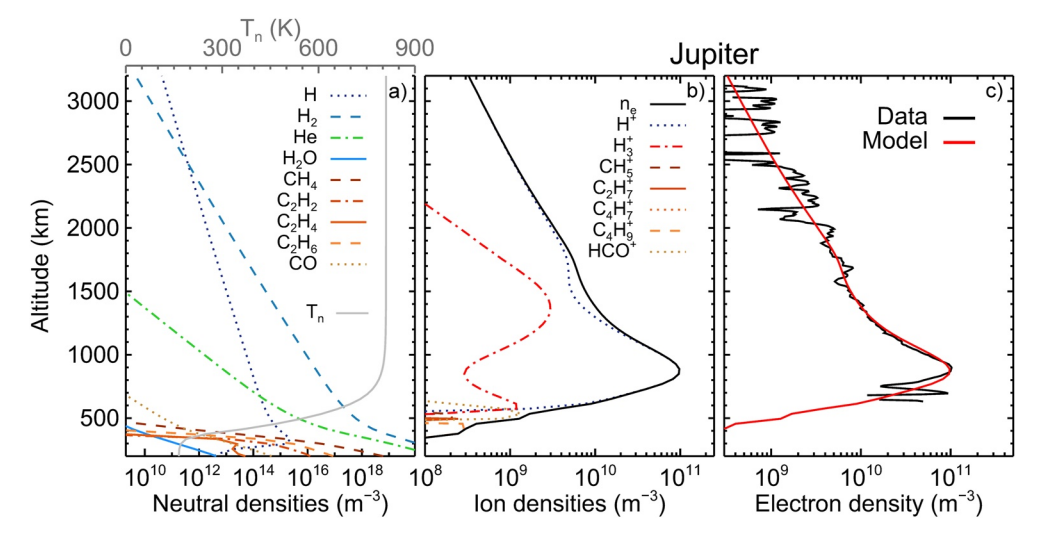


Figure 15. From (a–c), Jupiter neutral density and temperature structure; corresponding modeled ion densities; and the Galileo G0N radio occultation electron density profile (black) (Hinson et al., 1997) compared with the model reproduction (red).

MENDILLO ET AL. 22 of 25



9. Do revisions to our understanding of Jovian ionospheric physics provide comparative ionosphere feedback to prior studies of other giant planet ionospheres?

Data Availability Statement

Radio occultation data from Pioneer, Voyager, and Galileo were digitized by using WebPlotDigitizer (Rohatgi, 2021). The generated data set can now be found at this site https://hdl.handle.net/2144/43832 (Narvaez, 2022). Electron density profiles from radio occultations done by Galileo are from Hinson (2000). Solar flux F10.7 values from King and Papitashvili (2005) were obtained from the GSFC/SPDF OMNIWeb interface at https://omniweb.gsfc.nasa.gov/form/dx1.html. Earth ionosonde data were found in the UK Solar System Data Centre at https://www.ukssdc.ac.uk/wdcc1/iiwg_menu.html. Registration is required to retrieve data from the UK Solar System Data Centre.

Acknowledgments

Work at Boston University was possible through the support for comparative ionosphere studies from the NSF INSPIRE grant AST-1545581 and for aeronomy studies through NSF grant AGS-2035267. L. Moore was additionally supported by the National Aeronautics and Space Administration (NASA) under Grant 80NSSC20K1045 issued through the Solar System Workings Program. The authors are grateful to David Hinson for providing us with images of the Galileo radio occultation profiles. The authors thank Sophie Phillips for her assistance with the analysis of the terrestrial ionosonde data and Marissa Vogt for references giving the auroral boundaries shown in Figure 12.

References

- Atreya, S., Donahue, T., & Waite, J. (1979). An interpretation of the Voyager measurement of Jovian electron density profiles. *Nature*, 280(5725), 795–796. https://doi.org/10.1038/280795a0
- Bates, D. R., & Massey, H. S. W. (1946). The basic reactions in the upper atmosphere. *Proceedings of the Royal Society of London. Series A. Mathematical and Physical Sciences*, 187, 261–296. https://doi.org/10.1098/rspa.1946.0078
- Bates, D. R., & Massey, H. S. W. (1947). The basic reactions in the upper atmosphere II. The theory of recombination in the ionized layers. Proceedings of the Royal Society of London. Series A. Mathematical and Physical Sciences, 192, 1–16. https://doi.org/10.1098/rspa.1947.0134 Bauer, S. J., & Lammer, H. (2004). Planetary aeronomy. Springer.
- Bonfond, B., Saur, J., Grodent, D., Badman, S. V., Bisikalo, D., Shematovich, V., et al. (2017). The tails of the satellite auroral footprints at Jupiter. Journal of Geophysical Research: Space Physics, 122(8), 7985–7996. https://doi.org/10.1002/2017JA024370
- Campbell, B. A., & Watters, T. R. (2016). Phase compensation of MARSIS subsurface sounding data and estimation of ionospheric properties: New insights from SHARAD results. *Journal of Geophysical Research: Planets*, 121(2), 180–193. https://doi.org/10.1002/2015JE004917
- Cartacci, M., Amata, E., Cicchetti, A., Noschese, R., Giuppi, S., Langlais, B., et al. (2013). Mars ionosphere total electron content analysis from MARSIS subsurface data. *Icarus*, 223(1), 423–437. https://doi.org/10.1016/j.icarus.2012.12.011
- Chapman, S. (1931a). The production of ionization of monochromatic radiation incident upon a rotating atmosphere, Part I. *Proceedings of the Physical Society*, 43(1), 26–45. https://doi.org/10.1088/0959-5309/43/1/305
- Chapman, S. (1931b). The production of ionization of monochromatic radiation incident upon a rotating atmosphere, Part II. *Proceedings of the Physical Society*, 43(5), 483–501. https://doi.org/10.1088/0959-5309/43/5/302
- Chen, R. H. (1981). Studies of Jupiter's lower ionospheric layers. *Journal of Geophysical Research*, 86(A9), 7792–7794. https://doi.org/10.1029/ JA086iA09p07792
- Cravens, T. E. (1987). Vibrationally excited molecular hydrogen in the upper atmosphere of Jupiter. *Journal of Geophysical Research*, 92(A10), 11083–111000. https://doi.org/10.1029/ja092ia10p11083
- Dinelli, B., Fabiano, F., Adriani, A., Altieri, F., Moriconi, M., Mura, A., et al. (2017). Preliminary JIRAM results from Juno polar observations: 1. Methodology and analysis applied to the Jovian northern polar region. Geophysical Research Letters, 44(10), 1–8. https://doi.org/10.1002/2017GL072929
- Egert, A., Waite, J. H., & Bell, J. (2017). Applications of the Jupiter Global Ionosphere-Thermosphere Model: A case study of auroral electron energy deposition. *Journal of Geophysical Research: Space Physics*, 122(2), 2210–2236. https://doi.org/10.1002/2016JA023189
- Eshleman, V. R., Tyler, G. L., Wood, G. E., Lindal, G. F., Anderson, J. D., Levy, G. S., & Croft, T. A. (1979). Radio science with Voyager 1 at Jupiter: Preliminary profiles of the atmosphere and ionosphere. *Science*, 204(4396), 976–978. https://doi.org/10.1126/science.204.4396.976
- Fjeldbo, G., Kliore, A., Seidel, B., Sweetnam, D., & Cain, D. (1975). The Pioneer 10 radio occultation measurements of the ionosphere of Jupiter. Astronomy & Astrophysics, 39, 91–96.
- Gérard, J. C., Gkouvelis, L., Bonfond, B., Grodent, D., Gladstone, G. R., Hue, V., et al. (2020). Spatial Distribution of the Pedersen conductance in the Jovian aurora from Juno-UVS spectral images. *Journal of Geophysical Research: Space Physics*, 125(8), 1–11. https://doi.org/10.1029/2020JA028142
- Gurnett, D. A., Kirchner, D. L., Huff, R. L., Morgan, D. D., Persoon, A. M., Averkamp, T. F., et al. (2005). Radar soundings of the ionosphere of Mars. Science, 310(5756), 1929–1933. https://doi.org/10.1126/science.1121868
- Hinson, D. P. (2000). GO-J-RSS-5-ROCC-V1.0, GLL RPT ionosphere profiles [Data set]. NASA Planetary Data System. https://doi. org/10.17189/1519685
- Hinson, D. P., Flasar, F. M., Kliore, A. J., Schinder, P. J., Twicken, J. D., & Herrera, R. G. (1997). Jupiter's ionosphere: Results from the first Galileo radio occultation experiment. *Geophysical Research Letters*, 24(17), 2107–2110. https://doi.org/10.1029/97g101608
- Hinson, D. P., Simpson, R. A., Twicken, J. D., Tyler, G. L., & Flasar, F. M. (1999). Initial results from radio occultation measurements with Mars Global Surveyor. *Journal of Geophysical Research*, 104(E11), 26997–27012. https://doi.org/10.1029/1999JE001069
- Hinson, D. P., Twicken, J. D., & Karayel, E. T. (1998). Jupiter's ionosphere: New results from Voyager 2 radio occultation measurements. *Journal of Geophysical Research*, 103(A5), 9505–9520. https://doi.org/10.1029/97JA03689
- Kelley, M. C. (1989). The Earth's ionosphere. Plasma physics and electrodynamics. Academic Press.
- King, J. H., & Papitashvili, N. E. (2005). Solar wind spatial scales in and comparisons of hourly Wind and ACE plasma and magnetic field data. Journal of Geophysical Research, 110(A2), A02104. https://doi.org/10.1029/2004JA010649
- Kliore, A., Cain, D. L., Levy, G. S., Eshleman, V. R., Fjeldbo, G., & Drakem, F. D. (1965). Occultation experiment: Results of the first direct measurement of Mars's atmosphere and ionosphere. *Science*, 149(3689), 1243–1248. https://doi.org/10.1126/science.149.3689.1243
- Kliore, A., Levy, G. S., Cain, D. L., Fjeldbo, G., & Rasool, S. I. (1967). Atmosphere and ionosphere of Venus from the Mariner V S-band radio occultation measurement. Science, 158(3809), 1683–1688. https://doi.org/10.1126/science.158.3809.1683
- Kuiper, G. (1952). The atmospheres of the Earth and planets (2nd ed.). University of Chicago Press.

MENDILLO ET AL. 23 of 25



- Lindal, G. F., Wood, G. E., Levy, G. S., Anderson, J. D., Sweetnam, D. N., Hotz, H. B., et al. (1981). The atmosphere of Jupiter: An analysis of the Voyager radio occultation measurements. *Journal of Geophysical Research*, 86(A10), 8721–8727. https://doi.org/10.1029/JA086iA10p08721
- Lystrup, M. B., Miller, S., Dello Russo, N., Vervack, R. J. J., & Stallard, T. (2008). First vertical ion density profile in Jupiter's auroral atmosphere: Direct observations using the Keck II telescope. *The Astrophysical Journal*, 677(1), 790–797. https://doi.org/10.1086/529509
- Mahajan, K. K. (1981). Equatorial anomaly in the Jovian ionosphere. Geophysical Research Letters, 8(1), 66–68. https://doi.org/10.1029/gl008i001p00066
- Majeed, T., McConnell, J. C., & Gladstone, G. R. (1999). A model analysis of Galileo electron densities on Jupiter. Geophysical Research Letters, 26(15), 2335–2338. https://doi.org/10.1029/1999g1900530
- Majeed, T., Waite, J. H., Bougher, S. W., Yelle, R. V., Gladstone, G. R., McConnell, J. C., & Bhardwaj, A. (2004). The ionospheres-thermospheres of the giant planets. *Advances in Space Research*, 33(2), 197–211. https://doi.org/10.1016/j.asr.2003.05.009
- Matcheva, K., Strobel, D. F., & Flasar, F. M. (2001). Interaction of gravity waves with ionospheric plasma: Implications for Jupiter's ionosphere. Icarus, 152(2), 347–365. https://doi.org/10.1006/icar.2001.6631
- Materassi, M., Forte, B., Coster, A. J., & Skone, S. (2019). The dynamical ionosphere: A systems approach to ionospheric irregularity (1st ed.). Elsevier Science.
- Maurellis, A., & Cravens, T. (2001). Ionospheric effects of comet shoemaker–Levy 9 impacts with Jupiter. Icarus, 154(2), 350–371. https://doi.org/10.1006/jcar.2001.6709
- McConnell, J., Holberg, J., Smith, G., Sandel, B., Shemansky, D., & Broadfoot, L. (1982). A new look at the ionosphere of Jupiter in light of the UVS occultation results. *Planetary and Space Science*, 30(2), 151–167. https://doi.org/10.1016/0032-0633(82)90086-1
- Mendillo, M., Marusiak, A., Withers, P., Morgan, D., & Gurnett, D. (2013). A new semi-empirical model of the peak electron density of the Martian ionosphere. Geophysical Research Letters, 40(20), 5361–5365, https://doi.org/10.1002/2013GL057631
- Mendillo, M., Narvaez, C., & Campbell, B. (2017). The total electron content of the Martian ionosphere from MRO/SHARAD observations. Journal of Geophysical Research: Planets, 122(10), 2182–2192. https://doi.org/10.1002/2017JE005391
- Mendillo, M., Pi, X., Smith, S., Martinis, C., Wilson, J., & Hinson, D. (2004). Ionospheric effects upon a satellite navigation system at Mars. Radio Science, 39(2), RS2028. https://doi.org/10.1029/2003RS002933
- Mendillo, M., Trovato, J., Moore, L., & Müller-Wodarg, I. (2018). Comparative ionospheres: Terrestrial and giant planets. *Icarus*, 303, 34–46. https://doi.org/10.1016/j.icarus.2017.12.033
- Mendillo, M., Trovato, J., Narvaez, C., Mayyasi, M., Moore, L., Vogt, M. F., et al. (2016). Comparative aeronomy: Molecular ionospheres at Earth and Mars. *Journal of Geophysical Research: Space Physics*, 121(10), 10269–10288. https://doi.org/10.1002/2016JA023097
- Mendillo, M., Trovato, J., Narvaez, C., Withers, P., Pätzold, M., Peter, K., et al. (2020). The ionosphere of Venus: Strongest control by photo-chemical-equilibrium in the solar system, with implications for exospheric temperatures. *Icarus*, 349, 113870. https://doi.org/10.1016/j.icarus.2020.113870
- Migliorini, A., Dinelli, B. M., Moriconi, M. L., Altieri, F., Adriani, A., Mura, A., et al. (2019). H₃⁺ characteristics in the Jupiter atmosphere as observed at limb with Juno/JIRAM. *Icarus*, 329, 132–139. https://doi.org/10.1016/j.icarus.2019.04.003
- Miller, S., Tennyson, J., Geballe, T. R., & Stallard, T. (2020). Thirty years of H₃⁺ astronomy. Reviews of Modern Physics, 92(3), 035003. https://doi.org/10.1103/RevModPhys.92.035003
- Moore, L., Cravens, T. E., Müller-Wodarg, I., Perry, M. E., Waite, J. H., Jr, Perryman, R., et al. (2018). Models of Saturn's equatorial ionosphere based on in situ data from Cassini's Grand Finale. *Geophysical Research Letters*, 45(18), 9398–9407. https://doi.org/10.1029/2018GL078162
- Moore, L., Melin, H., O'Donoghue, J., Stallard, T., Moses, J., Galand, M., et al. (2019). Modeling H₃⁺ in planetary atmospheres: Effects of vertical gradients on observed quantities. *Philosophical Transactions of the Royal Society A*, 377(2154), 20190067. https://doi.org/10.1098/rsta.2019.0067
- Mura, A., Adriani, A., Altieri, F., Connerney, J. E. P., Bolton, S. J., Moriconi, M. L., et al. (2017). Infrared observations of Jovian aurora from Juno's first orbits: Main oval and satellite footprints. *Geophysical Research Letters*, 44(11), 5308–5316. https://doi.org/10.1002/2017GL072954
- Nagy, A. F., & Cravens, T. E. (2002). Solar system ionospheres. In M. Mendillo, A. Nagy, & J. Waite (Eds.), Atmospheres in the solar system: Comparative aeronomy. https://doi.org/10.1029/130GM04
- $Narvaez, C.\ (2022).\ Pioneer-Voyager-Galileo\ radio\ occultations\ [Data\ set].\ OpenBU.\ https://hdl.handle.net/2144/43832$
- Nichols, J. D., Clarke, J. T., Gérard, J. C., Grodent, D., & Hansen, K. C. (2009). Variation of different components of Jupiter's auroral emission. Journal of Geophysical Research, 114(A6), A06210. https://doi.org/10.1029/2009JA014051
- O'Donoghue, J., Moore, L., Bhakyapaibul, T., Melin, H., Stallard, T., Connerney, J. E. P., & Tao, C. (2021). Global upper-atmospheric heating on Jupiter by the polar aurorae. *Nature*, 596(7870), 54–57. https://doi.org/10.1038/s41586-021-03706-w
- Picardi, G., Plaut, J. J., Biccari, D., Bombaci, O., Calabrese, D., Cartacci, M., et al. (2005). Radar soundings of the subsurface of Mars. Science, 310(5756), 1925–1928, https://doi.org/10.1126/science.1122165
- Rishbeth, H. (1959). The ionosphere of Jupiter. Australian Journal of Physics, 12(4), 466-468. https://doi.org/10.1071/PH590466
- Rishbeth, H., & Garriott, O. K. (1969). Introduction to ionospheric physics. Academic Press.
- Rishbeth, H., & Mendillo, M. (2004). Ionospheric layers of Mars and Earth. Planetary and Space Science, 52(9), 849–852. https://doi.org/10.1016/j.pss.2004.02.007
- Rohatgi, A. (2021). WebPlotDigitizer (Version 4.5) [Computer software]. WebPlotDigitizer Online Software. Retrieved from https://automeris.io/WebPlotDigitizer
- Safaeinili, A., Kofman, W., Mouginot, J., Gim, Y., Herique, A., Ivanov, A. B., et al. (2007). Estimation of the total electron content of the Martian ionosphere using radar sounder surface echoes. Geophysical Research Letters, 34(23), L23204. https://doi.org/10.1029/2007GL032154
- Safaeinili, A., Kofman, W., Nouvel, J., Herique, A., & Jordan, R. L. (2003). Impact of Mars ionosphere on orbital radar sounder operation and data processing. *Planetary and Space Science*, 51(7–8), 505–515. https://doi.org/10.1016/S0032-0633(03)00048-5
- Schunk, R. W., & Nagy, A. F. (2009). Ionospheres (2nd ed.). Cambridge University Press. https://doi.org/10.1017/CBO9780511635342
- Stallard, T. S., Burrell, A. G., Melin, H., Fletcher, L. N., Miller, S., Moore, L., et al. (2018). Identification of Jupiter's magnetic equator through H₃+ ionospheric emission. *Nature Astronomy*, 2(10), 773–777. https://doi.org/10.1038/s41550-018-0523-z
- Strobel, D. F., & Atreya, S. K. (1983). Physics of the Jovian magnetosphere (A83-26611 10-91). Cambridge University Press.
- Uno, T., Kasaba, Y., Tao, C., Sakanoi, T., Kagitani, M., Fujisawa, S., et al. (2014). Vertical emissivity profiles of Jupiter's northern H₃⁺ and H₂ infrared auroras observed by Subaru/IRCS. *Journal of Geophysical Research: Space Physics*, 119(12), 10219–10241. https://doi.org/10.1002/2014JA020454
- Waite, J. H., & Cravens, T. E. (1987). Current review of the Jupiter, Saturn, and Uranus ionospheres. Advances in Space Research, 7(12), 119–134. https://doi.org/10.1016/0273-1177(87)90210-9
- Waite, J. H., Cravens, T. E., Kozyra, J., Nagy, A. F., Atreya, S. K., & Chen, R. H. (1983). Electron precipitation and related aeronomy of the Jovian thermosphere and ionosphere. *Journal of Geophysical Research*, 88(A8), 6143–6163. https://doi.org/10.1029/JA088iA08p06143

MENDILLO ET AL. 24 of 25



- Waite, J. H., Waite, J. H., Jr, Gladstone, G. R., Lewis, W. S., Drossart, P., Cravens, T. E., et al. (1997). Equatorial X-ray emissions: Implications for Jupiter's high exospheric temperatures. *Science*, 276(5309), 104–108. https://doi.org/10.1126/science.276.5309.104
- Witasse, O., Cravens, T., Mendillo, M., Moses, J., Kliore, A., Nagy, A. F., & Breus, T. (2008). Solar system ionospheres. *Space Science Reviews*, 139(1–4), 235–265. https://doi.org/10.1007/s11214-008-9395-3
- Withers, P., Felici, M., Mendillo, M., Moore, L., Narvaez, C., Vogt, M. F., et al. (2020). The MAVEN Radio Occultation Science Experiment (ROSE). Space Science Reviews, 216(4), 61. https://doi.org/10.1007/s11214-020-00687-6
- Woo, R., & Yang, F. C. (1978). Measurements of the magnetic field orientation in the Jovian Ionosphere deduced from Pioneer 10 and 11 scintillation observations. *Journal of Geophysical Research*, 83(A11), 5245–5255. https://doi.org/10.1029/JA083iA11p05245
- Wright, J. (1960). A model of the F region above h_mF₂. Journal of Geophysical Research, 65(1), 185–191. https://doi.org/10.1029/JZ065i001p00185
 Yelle, R. V., & Miller, S. (2004). Jupiter's thermosphere and ionosphere. In F. Bagenal, T. E. Dowling, & W. B. McKinnon (Eds.), Jupiter: The planet, satellites and magnetosphere (pp. 185–218). Cambridge University Press.

MENDILLO ET AL. 25 of 25